Tensor-Train Thermo-Field Memory Kernels for Generalized Quantum Master Equations

Ningyi Lyu,[∇] Ellen Mulvihill,[∇] Micheline B. Soley, Eitan Geva,* and Victor S. Batista*

ACCESS | Metrics & More | Article Recommendations | Supporting Information

ABSTRACT: The generalized quantum master equation (GQME) approach provides a rigorous framework for deriving the exact equation of motion for any subset of electronic reduced density matrix elements (e.g., the diagonal elements). In the context of electronic dynamics, the memory kernel and inhomogeneous term of the GQME introduce the implicit coupling to nuclear motion and dynamics of electronic density matrix elements that are projected out (e.g., the off-diagonal elements), allowing for efficient quantum dynamics simulations. Here, we focus on benchmark quantum simulations of electronic dynamics in a spin-boson model system described by various types of GQMEs. Exact memory kernels and inhomogeneous terms are obtained from short-time quantum-mechanically exact tensor-train thermo-field dynamics (TT-TFD) simulations and are compared with those obtained from an approximate linearized semiclassical method, allowing for assessment of the accuracy of these approximate memory kernels and inhomogeneous terms. Moreover, we have analyzed the computational cost of the full and reduced-dimensionality GQMEs. The scaling of the computational cost is dependent on several factors, sometimes with opposite scaling trends. The TT-TFD memory kernels can provide insights on the main sources of inaccuracies of GQME approaches when combined with approximate input methods and pave the road for the development of quantum circuits that implement GQMEs on digital quantum computers.
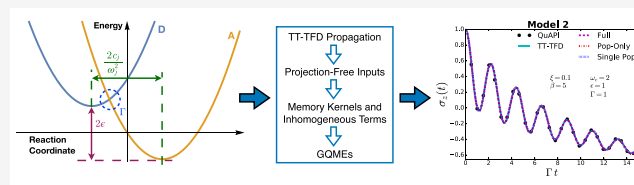
1. INTRODUCTION

Quantum dynamics simulations are central to theoretical studies of many areas of chemical and technological applications, including charge and energy transfer in photosynthetic and photovoltaic systems and a wide range of reactions with nonadiabatic dynamics and photochemical processes, including spin and vibrational energy relaxation, as well as polaritonic chemistry.[1−12] Despite considerable progress over the past few decades, the development of efficient methods for simulations of quantum dynamics remains an outstanding challenge for studies of complex molecular systems at finite temperature.[13−26] This is primarily due to the computational cost of quantum-mechanically exact simulations, which scales exponentially with the number of degrees of freedom in the system, thereby making such simulations intractable in most complex molecular systems of practical interest. Thus, reduced-dimensionality approaches that can offer more favorable scaling are highly desirable.

The Nakajima−Zwanzig generalized quantum master equation (GQME)[17,18] provides a formally exact general-purpose framework for modeling quantum dynamics in reduced dimensionality. It can be obtained for any subset of reduced density matrix elements by using suitable projection operators.[19] When focusing on electronic dynamics, the effect of projecting out nuclear degrees of freedoms (DOFs) and electronic density matrix elements not included in the subset of interest is accounted for by the *memory kernel* and the *inhomogeneous term* of the GQME. The dimensionality of those

spatially and temporally compact quantities is typically much lower than the dimensionality of the overall system since it is determined by the number of reduced density matrix elements included in the subset of interest, allowing for efficient simulations.

Considerable progress has already been made toward calculating the aforementioned memory kernels and inhomogeneous terms without resorting to perturbation theory.[19,27−52] Much of that progress has been based on the strategy introduced by Shi and Geva,[27] which relies on formally exact relationships between the memory kernel and the inhomogeneous term and projection-free inputs (PFIs) that are given in terms of two-time correlation functions of the overall system. These PFIs can be obtained from quantum-mechanically exact or approximate (e.g., semiclassical or mixed quantum-classical) input methods.[19,27−50,52]

In this paper, we introduce exact memory kernels and inhomogeneous terms obtained from quantum-mechanically exact tensor-train thermo-field dynamics (TT-TFD) simulations.[53,54] To the best of our knowledge, this is the first

application of TT-TFD to calculate memory kernels and inhomogeneous terms of GQMEs. Previously, exact memory kernels have been obtained by the Geva,[27] Shi,[47−50] Makri,[51] and Rabani[31,33,34,36,55] groups. This paper extends the available exact results to include the memory kernels and inhomogeneous terms of the modified GQME and reduced-dimensionality GQME approaches for the spin-boson model. We demonstrate the capabilities of the GQMEs as applied to benchmark simulations of electronic relaxation dynamics in a spin-boson model system, including calculations based on various types of reduced-dimensionality GQMEs. The spin-boson model provides a useful framework for modeling molecular systems with coupled electronic states. The resulting quantum-mechanically exact memory kernels and inhomogeneous terms can serve as benchmarks for assessing the accuracy of approximate memory kernels and inhomogeneous terms obtained by approximate input methods. In addition, the reported quantum-mechanically exact memory kernels and inhomogeneous terms enables the development of quantum circuits for the implementation of GQMEs on digital quantum computers, which we report in the upcoming work.[56]

The paper is organized as follows. The objectives and scope of our approach are presented in Section 2, the GQME formalism is outlined in Section 3, and the protocol used for calculating the PFIs via TT-TFD is described in Section 4. The utility of combining the GQME and TT-TFD approaches is demonstrated for the benchmark spin-boson model in Section 5. Also included in Section 5 is a comprehensive comparison between the TT-TFD-based quantum-mechanically exact results and the corresponding approximate results based on PFIs obtained with an approximate linearized semiclassical mapping Hamiltonian method.[19] Concluding remarks are provided in Section 6. Additional graphs and computational details are included in the Supporting Information (SI).

2. MODEL SYSTEM

We focus on molecular systems exhibiting nonadiabatic quantum dynamics such as photosynthetic and photovoltaic molecular assemblies, commonly described by the following model Hamiltonian:

$$\hat{H} = \sum_{j=1}^{N_e} \hat{H}_j |j\rangle\langle j| + \sum_{\substack{j,k=1 \\ j\neq k}}^{N_e} \hat{V}_{jk} |j\rangle\langle k| \tag{1}$$

Here, $\hat{H}_j$ is the nuclear Hamiltonian when the system is in diabatic electronic state $|j\rangle$ $[\hat{H}_j = \hat{\mathbf{P}}^2/2 + V_j(\hat{\mathbf{R}})]$, with index j running over the N_e electronic states ($j = 1, 2, ..., N_e$), while $\hat{\mathbf{R}} = (\hat{R}_1, ..., \hat{R}_{N_n})$ and $\hat{\mathbf{P}} = (\hat{P}_1, ..., \hat{P}_{N_n})$ are the mass-weighted position and momentum operators of the $N_n \gg 1$ nuclear DOF, and $\{\hat{V}_{jk} |j \neq k\}$ are coupling terms between electronic states which can be either nuclear operators (non-Condon case) or constants (Condon case). Throughout this paper, a circumflex symbol over a variable (e.g., $\hat{B}$) indicates an operator quantity and a script font (e.g., $\mathcal{L}$) indicates a superoperator.

For simplicity, we assume that the initial state of the overall system has the single-product form,

$$\hat{\rho}(0) = \hat{\rho}_n(0) \otimes \hat{\sigma}(0) \tag{2}$$

Here, $\hat{\rho}_n(0) = \mathrm{Tr}_e\{\hat{\rho}(0)\}$ and $\hat{\sigma}(0) = \mathrm{Tr}_n\{\hat{\rho}(0)\}$ are the reduced density operators that describe the initial states of nuclear DOF and electronic DOF, respectively, while $\mathrm{Tr}_e\{\cdot\}$ and $\mathrm{Tr}_n\{\cdot\}$ represent partial traces over the electronic and nuclear Hilbert spaces, respectively. The methodology presented in this paper is not limited to factorized initial states, as introduced by eq 2, and can be applied to arbitrary initial states.[43]

The time-dependent propagation of the initial state, introduced by eq 2, according to the Hamiltonian introduced by eq 1, yields the propagated state $\hat{\rho}(t)$ at time t, which is described by the following density operator:

$$\hat{\rho}(t) = e^{-i\hat{H}t/\hbar}\hat{\rho}_n(0) \otimes \hat{\sigma}(0)e^{i\hat{H}t/\hbar} \equiv e^{-i\mathcal{L}t/\hbar}\hat{\rho}_n(0) \otimes \hat{\sigma}(0) \tag{3}$$

Here, $\mathcal{L}(\cdot)$ is the overall Liouvillian superoperator ($\mathcal{L}(\cdot) = [\hat{H}, \cdot]$). The reduced electronic density operator $\hat{\sigma}(t)$ at time t is obtained by tracing out the nuclear, as follows:

$$\hat{\sigma}(t) = \mathrm{Tr}_n\{\hat{\rho}(t)\} = \sum_{j,k=1}^{N_e} \sigma_{jk}(t)|j\rangle\langle k| \tag{4}$$

The electronic populations and coherences are given by $\{\sigma_{jj}(t) = \langle j|\hat{\sigma}(t)|j\rangle\}$ and $\{\sigma_{jk}(t) = \langle j|\hat{\sigma}(t)|k\rangle|j \neq k\}$, respectively. These quantities are of particular interest, because their time evolution underlies electronic energy, charge, and coherence transfer dynamics, as well as electronic decoherence.

3. GQMES IN REDUCED DIMENSIONALITY

The GQME formalism can be applied to derive exact equations of motion for electronic observables while keeping the input regarding other DOFs in the system to the minimum necessary to account for their impact on dynamics. To this end, we begin with the well-known Nakajima−Zwanzig GQME (whose derivation is outlined in the SI),

$$\frac{\mathrm{d}}{\mathrm{d}t}\mathcal{P}\hat{\rho}(t) = -\frac{i}{\hbar}\mathcal{P}\mathcal{L}\mathcal{P}\hat{\rho}(t) - \frac{1}{\hbar^2}\int_0^t \mathrm{d}\tau\, \mathcal{P}\mathcal{L}e^{-iQ\mathcal{L}\tau/\hbar}Q\mathcal{L}\mathcal{P}\hat{\rho}(t-\tau)$$
$$-\frac{i}{\hbar}\mathcal{P}\mathcal{L}e^{-iQ\mathcal{L}t/\hbar}Q\hat{\rho}(0) \tag{5}$$

where $\mathcal{P}$ is a projection superoperator.[17,18] Here, Q is the projection superoperator complementary to $\mathcal{P}$ ($Q = \mathcal{I} - \mathcal{P}$), $\mathcal{I}$ is the identity superoperator, and $\mathcal{L}$ is the Liouvillian superoperator as in eq 3. Integrating eq 5, we obtain the time-dependent projected state $\mathcal{P}\hat{\rho}(t)$. Importantly, there is a lot of flexibility in the choice of $\mathcal{P}$ to select the specific quantity of interest.[19]

In this paper, we focus on quantities of interest corresponding to a subset of electronic reduced density matrix elements $\{\sigma_{ab}(t)\}$. For example, $\{\sigma_{ab}(t)\}$ may include all N_e^2 electronic reduced density matrix elements (i.e., all populations and coherences), in which case $\{\sigma_{ab}(t)\} = \{\sigma_{11}(t), ..., \sigma_{1N_e}(t), ..., \sigma_{N_e 1}(t), ..., \sigma_{N_e N_e}(t)\}$; or only the diagonal electronic reduced density matrix elements (i.e., the populations of the corresponding electronic states), in which case $\{\sigma_{ab}(t)\} = \{\sigma_{11}(t), ..., \sigma_{N_e N_e}(t)\}$; or just the single diagonal term describing the time-dependent population of state $|1\rangle$, in which case $\{\sigma_{ab}(t)\} = \{\sigma_{11}(t)\}$. The GQME of an element $\sigma_{jk}(t)$ in a specific subset of electronic reduced density matrix elements $\{\sigma_{ab}(t)\}$ is defined as

$$\frac{d}{dt}\sigma_{jk}(t) = -\frac{i}{\hbar}\sum_{lm\in\{ab\}}\langle\mathcal{L}_{jk,lm}\rangle_n^0\sigma_{lm}(t)$$
$$-\sum_{lm\in\{ab\}}\int_0^t d\tau\,\mathcal{K}_{jk,lm}^{set}(\tau)\sigma_{lm}(t-\tau) + \hat{I}_{jk}^{set}(t) \tag{6}$$

Equation 6 is different for different subsets of electronic reduced density matrix elements. It can be obtained by first defining the projection superoperator

$$\mathcal{P}^{set}\hat{A} = \sum_{jk\in\{ab\}}\text{Tr}\{(|j\rangle\langle k|\otimes\hat{1}_n)^\dagger\hat{A}\}\hat{\rho}_n(0)\otimes|j\rangle\langle k| \tag{7}$$

where $\hat{A}$ is a general overall system operator, $\{ab\}$ are the indices matching the subset of electronic reduced density matrix elements $\{\sigma_{ab}(t)\}$, and $\hat{1}_n$ is the unity operator in the nuclear Hilbert space. Equation 6 can then be obtained by substituting the projection superoperator $\mathcal{P}^{set}$ defined in eq 7 into eq 5, tracing over the nuclear Hilbert spaces, and applying $\langle j|$ from the left and $|k\rangle$ from the right, with a detailed derivation included in the SI (section S.I.2). Note that, because the sum in eq 7 goes over the elements of the subset of interest, $\mathcal{P}^{set}$ will be different for different subsets and, therefore, the equation of motion in eq 6 will also be different, *even for the same element when it is in different subsets.* For example, if we are looking at one subset $\{\sigma_{ab}(t)\} = \{\sigma_{11}(t)\}$ and another subset $\{\sigma_{ab}(t)\} = \{\sigma_{11}(t),\ \sigma_{12}(t)\}$, the equation of motion for $\sigma_{11}(t)$ given in eq 6 will be different for the first subset versus the second subset. These different equations of motion are exact, so if exact input methods are used to obtain the terms on the right-hand side (RHS) of eq 6 for $\sigma_{11}(t)$, the results will be the same. However, if approximate input methods are used, the results can differ.[19]

In eq 6, $\langle\mathcal{L}_{jk,lm}\rangle_n^0$, $\mathcal{K}_{jk,lm}^{set}(\tau)$, and $\hat{I}_{jk}^{set}(t)$ are the matrix elements (jk, lm) of the *projected Liouvillian* superoperator, *memory kernel* superoperator, and *inhomogeneous term* operator, respectively, which are defined as follows:

$$\langle\mathcal{L}_{jk,lm}\rangle_n^0 = \text{Tr}\{(|j\rangle\langle k|\otimes\hat{1}_n)^\dagger\mathcal{L}\hat{\rho}_n(0)\otimes|l\rangle\langle m|\} \tag{8}$$

$$\mathcal{K}_{jk,lm}^{set}(\tau) = \frac{1}{\hbar^2}\text{Tr}\{(|j\rangle\langle k|\otimes\hat{1}_n)^\dagger\mathcal{L}\,e^{-iQ^{set}\mathcal{L}\tau/\hbar}Q^{set}\mathcal{L}\hat{\rho}_n(0)\otimes|l\rangle\langle m|\} \tag{9}$$

and

$$\hat{I}_{jk}^{set}(t) = -\frac{i}{\hbar}\text{Tr}\Bigg\{(|j\rangle\langle k|\otimes\hat{1}_n)^\dagger\mathcal{L}\,e^{-iQ^{set}\mathcal{L}t/\hbar}$$
$$\times\Bigg[\hat{\rho}(0) - \sum_{lm\in\{ab\}}\hat{\rho}_n(0)\otimes|l\rangle\langle m|\sigma_{lm}(0)\Bigg]\Bigg\} \tag{10}$$

These quantities are subset-dependent, so they will differ depending on the chosen subset of electronic density matrix elements of interest. Given that N_{set} is the number of matrix elements of interest included in $\{\sigma_{ab}(t)\}$ ($1 \le N_{set} \le N_e^2$), the projected Liouvillian $\langle\mathcal{L}\rangle_n^0$ and memory kernel $\mathcal{K}^{set}(\tau)$ superoperators can be represented by $N_{set}\times N_{set}$ matrices, whereas the inhomogeneous term operator $\hat{I}^{set}(t)$ can be represented by an N_{set}-dimensional vector in Liouville space.

Calculating the projected Liouvillian is typically straightforward. The memory kernel and inhomogeneous term satisfy Volterra integral equations, so they can be obtained from the PFIs.[19] The Volterra equation for the memory kernel is given by

$$\mathcal{K}_{jk,lm}^{set}(\tau) = i\dot{\mathcal{F}}_{jk,lm}(\tau) - \frac{1}{\hbar}\sum_{uv\in\{ab\}}\mathcal{F}_{jk,uv}(\tau)\langle\mathcal{L}_{uv,lm}\rangle_n^0$$
$$+ i\sum_{uv\in\{ab\}}\int_0^\tau d\tau'\,\mathcal{F}_{jk,uv}(\tau-\tau')\mathcal{K}_{uv,lm}^{set}(\tau') \tag{11}$$

where the PFIs are given by

$$\mathcal{F}_{jk,lm}(\tau) = \frac{1}{\hbar}\text{Tr}\{(|j\rangle\langle k|\otimes\hat{1}_n)^\dagger\mathcal{L}\,e^{-i\mathcal{L}\tau/\hbar}\hat{\rho}_n(0)\otimes|l\rangle\langle m|\}$$
$$\dot{\mathcal{F}}_{jk,lm}(\tau) = -\frac{i}{\hbar^2}\text{Tr}\{(|j\rangle\langle k|\otimes\hat{1}_n)^\dagger\mathcal{L}\,e^{-i\mathcal{L}\tau/\hbar}\mathcal{L}\hat{\rho}_n(0)\otimes|l\rangle\langle m|\} \tag{12}$$

The Volterra equation for the inhomogeneous term is given by

$$\hat{I}_{jk}^{set}(t) = \hat{Z}_{jk}(t) + i\sum_{lm\in\{ab\}}\mathcal{F}_{jk,lm}(t)\sigma_{lm}(0)$$
$$+ i\sum_{uv\in\{ab\}}\int_0^t d\tau\,\mathcal{F}_{jk,uv}(t-\tau)I_{uv}^{set}(\tau) \tag{13}$$

where the additional PFI $Z_{jk}(t)$ is given by

$$\hat{Z}_{jk}(t) = -\frac{i}{\hbar}\text{Tr}\{(|j\rangle\langle k|\otimes\hat{1}_n)^\dagger\mathcal{L}\,e^{-i\mathcal{L}t/\hbar}\hat{\rho}(0)\} \tag{14}$$

Note that $\hat{Z}_{jk}(t) = -i\mathcal{F}_{jk,\alpha\alpha}(t)$ when the overall initial state is of the commonly encountered form $\hat{\rho}(0) = \hat{\rho}_n(0)\otimes|\alpha\rangle\langle\alpha|$ (where $|\alpha\rangle$ is one of the electronic basis states), as is the case for the applications reported in this paper. A more-detailed discussion of the derivation, properties, and significance of eqs 11−14) can be found in ref 19 and in the SI.

Most previous studies have been based on direct calculations of the aforementioned PFIs.[19,43,43−46] However, when using an exact input method, the PFIs can also be accurately obtained as derivatives of the propagator $\mathcal{U}(\tau) \equiv \text{Tr}_n\{e^{-i\mathcal{L}\tau/\hbar}\hat{\rho}_n(0)\otimes\hat{1}_e\}$ that evolves the electronic reduced density operator, as follows:[41,43]

$$\hat{\sigma}(\tau) = \mathcal{U}(\tau)\hat{\sigma}(0) \tag{15}$$

with matrix elements,

$$\mathcal{U}_{jk,lm}(\tau) = \text{Tr}\{(|j\rangle\langle k|\otimes\hat{1}_n)^\dagger\,e^{-i\mathcal{L}\tau/\hbar}\hat{\rho}_n(0)\otimes|l\rangle\langle m|\} \tag{16}$$

Specifically, we obtain the PFIs $\{\mathcal{F}_{jk,lm}(\tau), \dot{\mathcal{F}}_{jk,lm}(\tau)\}$ from $\{\mathcal{U}_{jk,lm}(\tau)\}$, as follows:[41,43]

$$\mathcal{F}_{jk,lm}(\tau) = i\dot{\mathcal{U}}_{jk,lm}(\tau) \qquad \dot{\mathcal{F}}_{jk,lm}(\tau) = i\ddot{\mathcal{U}}_{jk,lm}(\tau) \tag{17}$$

PFIs $\{\mathcal{F}_{jk,lm}(\tau), \dot{\mathcal{F}}_{jk,lm}(\tau)\}$ calculated from $\mathcal{U}(\tau)$ generate exact memory kernels and inhomogeneous terms when $\mathcal{U}(\tau)$ is obtained from exact inputs. Therefore, we can calculate them in terms of numerical derivatives of $\mathcal{U}(\tau)$ obtained from quantum-mechanically exact TT-TFD simulations, as described in Section 4.

4. TENSOR-TRAIN THERMO-FIELD DYNAMICS

4.1. Hamiltonian. The molecular Hamiltonian introduced by eq 1 can also be written as the sum of a purely electronic Hamiltonian $\hat{H}_e \otimes \hat{1}_n$, plus a purely nuclear Hamiltonian $\hat{1}_e \otimes \hat{H}_n$, and an interaction term between the electronic and nuclear DOF, $\hat{H}_{en}$:

$$\hat{H} = \hat{H}_e \otimes \hat{1}_n + \hat{1}_e \otimes \hat{H}_n + \hat{H}_{en} \tag{18}$$

Note that this division is not unique, in the sense that different choices of $\hat{H}_e$, $\hat{H}_n$, and $\hat{H}_{en}$ are possible.[43] However, the results are invariant to those choices when a quantum-mechanically exact method like TT-TFD is applied, since no physical or ad hoc approximation is introduced.

4.2. Thermo-Field Dynamics Method. We start out by noting that the dynamics of $\hat{\rho}(t)$, which is governed by a Hamiltonian of the form of eq 18, is described by the quantum Liouville equation,

$$\frac{d}{dt}\hat{\rho}(t) = -\frac{i}{\hbar}[\hat{H}, \hat{\rho}(t)] \tag{19}$$

The TT-TFD method[53,54,57,58] provides a general, numerically exact approach to solve eq 19 that is particularly efficient when $\hat{\rho}(t)$ can be represented as a low rank matrix product state. In our simulations, the state is described by $\hat{\rho}^{1/2}(t)$ [instead of $\hat{\rho}(t)$], represented as a tensor-train vector in an extended Hilbert space (the so-called double Hilbert space described below). The Liouville equation given in eq 19 is replaced by an equivalent equation of motion for $\hat{\rho}^{1/2}(t)$, which can be written in the form of a Schrödinger-like equation in the double Hilbert space. For a high-dimensional system, computational efficiency is achieved by using a tensor-train representation[26,59−65] of the extended state vector $\hat{\rho}^{1/2}(t)$. The remainder of this section outlines the TT-TFD methodology used for calculating the PFIs needed to obtain the memory kernel and inhomogeneous term of the GQMEs.

The initial density operator of the overall system is of the form introduced by eq 2. The initial electronic density operator is given by $\hat{\sigma}(0) = |\gamma\rangle\langle\gamma|$, where $|\gamma\rangle$ is one of the electronic basis states, while the initial nuclear density operator is $\hat{\rho}_n(0) = e^{-\beta\hat{H}_n}/Z_n(\beta)$, where $Z_n(\beta) = \mathrm{Tr}_n\{e^{-\beta\hat{H}_n}\}$. Therefore,

$$\hat{\rho}(0) = |\gamma\rangle\langle\gamma| \otimes \frac{e^{-\beta\hat{H}_n}}{Z_n(\beta)} \tag{20}$$

However, we note that the TT-TFD method is not restricted to initial states of this simple form and can be analogously applied to propagate any arbitrary initial state.

The TFD representation is only applied to the nuclear density operator of the system, since the same dynamics is obtained for the initial state introduced by eq 20, regardless of whether the electronic density operator is included or not in the TFD representation.[57] We let $\{|k\rangle\}$ be an orthonormal basis that spans the *physical* nuclear Hilbert space $\mathfrak{H}_n$ and $\{|\tilde{k}\rangle\}$ be an orthonormal basis that spans a *fictitious* nuclear Hilbert space (also known as the tilde space) $\tilde{\mathfrak{H}}_n$, which is an exact replica of $\mathfrak{H}_n$. Next, we define the so-called *nuclear thermal vacuum state*:

$$|0_n(\beta)\rangle = \frac{e^{-\beta\hat{H}_n/2}}{\sqrt{Z(\beta)}}\sum_{\tilde{k}=k}|k\rangle \otimes |\tilde{k}\rangle \tag{21}$$

where one should note that the sum includes only terms $|k\rangle \otimes |\tilde{k}\rangle$ with $\tilde{k} = k$, so that $\sum_{\tilde{k}=k}|k\rangle \otimes |\tilde{k}\rangle = |0\rangle \otimes |\tilde{0}\rangle + |1\rangle \otimes |\tilde{1}\rangle + \ldots$. We note that $\hat{\rho}_n(0)$ can be obtained from $|0_n(\beta)\rangle$, upon taking the outer product with its dual and tracing out the fictional degrees of freedom as follows:

$$\mathrm{Tr}_f\{|0_n(\beta)\rangle\langle 0_n(\beta)|\} = \hat{\rho}_n(0) \tag{22}$$

where $\mathrm{Tr}_f\{\cdot\}$ is the partial trace over states $|\tilde{k}\rangle$ in the tilde space $\tilde{\mathfrak{H}}_n$.

Substituting eq 22 into eq 20, we obtain the initial density operator of the overall system $\hat{\rho}(0)$ represented in terms of the ket vector $|\psi_\gamma(\beta, 0)\rangle \equiv |\gamma\rangle \otimes |0_n(\beta)\rangle$, as follows:

$$\hat{\rho}(0) = \mathrm{Tr}_f\{|\psi_\gamma(\beta, 0)\rangle\langle\psi_\gamma(\beta, 0)|\} \tag{23}$$

Note that, in eq 23, only the initially thermalized nuclear density operator is represented by a ket vector in the double space $\tilde{\mathfrak{H}}_n \otimes \mathfrak{H}_n$, whereas the initial electronic density operator $|\gamma\rangle\langle\gamma|$ corresponds to a pure state in the electronic Hilbert space.

We define the overall system ket vector $|\psi_\gamma(\beta, t)\rangle$, such that

$$\hat{\rho}(t) = \mathrm{Tr}_f\{|\psi_\gamma(\beta, t)\rangle\langle\psi_\gamma(\beta, t)|\} \tag{24}$$

where $\hat{\rho}(t)$ evolves according to the Liouville equation (eq 19). This can be fulfilled by evolving $|\psi_\gamma(\beta, t)\rangle$ according to the so-called TFD Schrödinger equation (as shown in the SI),

$$\frac{d}{dt}|\psi_\gamma(\beta, t)\rangle = -\frac{i}{\hbar}\bar{H}|\psi_\gamma(\beta, t)\rangle \tag{25}$$

where $\bar{H} = \hat{H} \otimes \tilde{1}_n$, with $\tilde{1}_n = \sum_{\tilde{k}}|\tilde{k}\rangle\langle\tilde{k}|$ being the identity operator of the tilde space. Moreover, we note that the same physical system dynamics can be obtained by defining $\bar{H}$ in eq 25, as follows:

$$\bar{H} = \hat{H} \otimes \tilde{1}_n - \hat{1} \otimes \tilde{H}_n \tag{26}$$

where $\hat{1} = \hat{1}_n \otimes \hat{1}_e$. Remarkably, $\tilde{H}_n$ can be *any* operator in the nuclear tilde space since $\tilde{H}_n$ does not impact kets in the physical space and its effect on the dynamics vanishes upon taking the partial trace over states in the tilde space.[57]

The preparation of the initial thermal wavepacket $|\psi_\gamma(\beta, 0)\rangle$, according to eqs 21 and 22, requires the explicit evaluation of the quantum Boltzmann operator, which can be computationally challenging for systems with high dimensionality. However, when the initial nuclear Hamiltonian is harmonic, the initial thermal wavepacket can be obtained by taking advantage of the *thermal Bogoliubov transformation*. Therefore, we can generate the nuclear thermal vacuum state from the double space ground state $|0_n, \tilde{0}_n\rangle$ using the following unitary transformation:

$$|\psi_\gamma(\beta, 0)\rangle = |\gamma\rangle \otimes e^{-i\hat{G}}|0_n, \tilde{0}_n\rangle \tag{27}$$

where $\hat{G}$ is given by[53,54,66]

$$\hat{G} = -i\sum_j \theta_j(\hat{a}_j\tilde{a}_j - \hat{a}_j^\dagger\tilde{a}_j^\dagger) \tag{28}$$

with $\theta_j = \text{arctanh}(e^{-\beta\omega_j/2})$, where $\{\hat{a}_j, \hat{a}_j^\dagger\}$ and $\{\tilde{a}_j, \tilde{a}_j^\dagger\}$ are the creation and annihilation operators associated with the jth nuclear DOF in the physical and tilde Hilbert spaces, respectively.

Substituting eqs 27 and 28 into eq 25, we obtain

$$\frac{d}{dt}|\psi_{\theta,\gamma}(\beta, t)\rangle = -\frac{i}{\hbar}\bar{H}_\theta|\psi_{\theta,\gamma}(\beta, t)\rangle \tag{29}$$

with $|\psi_{\theta,\gamma}(\beta, 0)\rangle = |\gamma\rangle \otimes |0, \tilde{0}\rangle$, $|\psi_{\theta,\gamma}(\beta, t)\rangle = e^{i\hat{G}}|\psi_\gamma(\beta, t)\rangle$, and $\bar{H}_\theta$ is defined as

$$\bar{H}_\theta = e^{i\hat{G}}\bar{H}e^{-i\hat{G}} \tag{30}$$

The time-dependent thermal state $|\psi_{\theta,\gamma}(\beta,t)\rangle$ is represented as

$$|\psi_{\theta,\gamma}(\beta, t)\rangle = \sum_{j_1,\dots,j_d}^{n_1,\dots,n_d} X(\beta, t; j_1, \dots, j_d)|j_1\rangle \otimes \dots \otimes |j_d\rangle \tag{31}$$

where d is the overall number of DOF ($d = 1 + 2N_n$) and $\{|j_k\rangle\}$ is the basis set with $k = 1, \dots, d$. We determined the size of the basis according to the convergence test, including two electronic state eigenvectors and the 10 nuclear harmonic eigenvectors for the nuclear DOF.

The time- and temperature-dependent expansion coefficients $\{X(\beta, t; j_1, \dots, j_d)\}$ correspond to an $n_1 \times \dots \times n_d$ complex array which requires storage space and computational effort that grows exponentially with d. Thus, we avoid the curse of dimensionality by implementing the TFD wavepacket in the tensor-train (TT) format.[26,59−65]

4.3. TT Format. The TT format of $X \in \mathbb{C}^{n_1 \times \dots \times n_d}$ involves a trainlike product of d tensor cores, which are three-mode tensors, $X_i \in \mathbb{C}^{r_{i-1} \times n_i \times r_i}$, with $r_0 = r_d = 1$. Any particular element $X(j_1, \dots, j_d)$ can be evaluated by multiplication of the cores, as follows:

$$X(j_1, \dots, j_d) = \sum_{a_0=1}^{r_0} \sum_{a_1=1}^{r_1} \dots \sum_{a_d=1}^{r_d} X_1(a_0, j_1, a_1)X_2(a_1, j_2, a_2) \dots X_d(a_{d-1}, j_d, a_d) \tag{32}$$

This can also be written in compact matrix product notation, as follows:

$$X(j_1, \dots, j_d) = \mathbf{X}_1(j_1)\mathbf{X}_2(j_2)\dots\mathbf{X}_d(j_d) \tag{33}$$

with matrix $\mathbf{X}_i(j_i) \in \mathbb{C}^{r_{i-1} \times r_i}$ defining the j_ith slice of X_i.

The central idea of the TT format is to generalize the concept of factorization. Each physical dimension i is factorized as an individual core (i.e., X_i). Entanglement with other physical dimensions is established through the auxiliary indices a_{i-1} and a_i. The TT-ranks $r_0, \dots, r_d$ introduced by eq 32 remain small for a low level of entanglement and when they are $r_0 = \dots = r_d = 1$, the TT format of X is a factorizable product.

Equation 32 shows that the TT format allows for compressed representations of X, since it requires storage of $X_1, \dots, X_d$, with $dn\tilde{r}^2$ elements when $r_1 = \dots = r_{d-1} = \tilde{r}$ and $n_1 = \dots = n_d = n$. For small $\tilde{r}$, such a representation bypasses the need to explicitly store all n^d elements of X, thus offering an exponential advantage in storage and computational effort.

In TT-TFD, the initial state $|\psi_{\theta,\gamma}(\beta, 0)\rangle = |\gamma\rangle \otimes |0, \tilde{0}\rangle$ takes an initial single-product form and is prepared as a rank-1

tensor train. The transformed TFD Schrödinger equation is then solved with the TT-KSL method.[67,68] The TT-KSL propagator evolves the wavepacket according to the time-dependent variational principle (TDVP) by evolving the time-dependent state on a fixed-rank TT manifold. Comparisons to other TT propagators have shown that TT-KSL is quite accurate and efficient.[63,69]

4.4. Projection-Free Inputs from TT-TFD. The PFIs required for calculating the memory kernel and inhomogeneous term of the GQME are computed by using the TT-TFD methodology. According to eq 16, the matrix elements $\mathcal{U}_{jk,lm}(\tau)$ are obtained, as follows:

$$\mathcal{U}_{jk,lm}(\tau) = \text{Tr}_{e,n}\{e^{-i\hat{H}\tau/\hbar}\hat{\rho}_n(0)|l\rangle\langle m|e^{i\hat{H}\tau/\hbar}(|k\rangle\langle j| \otimes \hat{1}_n)\} \tag{34}$$

Since TT-TFD requires an initial electronic state that is in a pure state $|\gamma\rangle$, in the following, we write $|l\rangle\langle m|$ as $|\gamma\rangle\langle\gamma|$; however, we note that all $\mathcal{U}(\tau)$ elements with off-diagonal initial electronic density matrices can be expressed as linear combinations of pure-state populations (see the SI).

We use $|k\rangle\langle j|j\rangle\langle j| = |k\rangle\langle j|$ to rewrite $\mathcal{U}_{jk,\gamma\gamma}(\tau)$ as

$$\mathcal{U}_{jk,\gamma\gamma}(\tau) = \text{Tr}_{e,n}\{e^{-i\hat{H}\tau/\hbar}\hat{\rho}_n(0)|\gamma\rangle\langle\gamma|e^{i\hat{H}\tau/\hbar}(|k\rangle\langle j| \otimes \hat{1}_n)\}$$
$$= \text{Tr}_{e,n}\{e^{-i\hat{H}\tau/\hbar}\hat{\rho}_n(0)|\gamma\rangle\langle\gamma|e^{i\hat{H}\tau/\hbar}(|k\rangle\langle j| \otimes \hat{1}_n)(|j\rangle\langle j| \otimes \hat{1}_n)\} \tag{35}$$

From this equation, noting that $\text{Tr}_f\{|\psi_\gamma(\beta, \tau)\rangle\langle\psi_\gamma(\beta, \tau)|\} = e^{-i\hat{H}\tau/\hbar}\hat{\rho}_n(0)|\gamma\rangle\langle\gamma|e^{i\hat{H}\tau/\hbar}$, we perform a cyclic permutation to obtain

$$\mathcal{U}_{jk,\gamma\gamma}(\tau) = \text{Tr}_{e,n}\{\text{Tr}_f\{(|j\rangle\langle j| \otimes \hat{1}_n)|\psi_\gamma(\beta, t)\rangle\langle\psi_\gamma(\beta, \tau)|(|k\rangle\langle j| \otimes \hat{1}_n)\}\} \tag{36}$$

From here, we use $|\psi_{jk,\gamma\gamma}(\tau)\rangle = (|k\rangle\langle j| \otimes \hat{1}_n)|\psi_\gamma(\beta, \tau)\rangle$ and $|\psi_{\theta,jk\gamma\gamma}(\tau)\rangle = e^{iG}|\psi_{jk,\gamma\gamma}(\tau)\rangle = (|k\rangle\langle j| \otimes \hat{1}_n|)\psi_{\gamma,\theta}(\beta, \tau)\rangle$ to obtain

$$\mathcal{U}_{jk,\gamma\gamma}(\tau) = \text{Tr}_{e,n,f}\{|\psi_{jj,\gamma\gamma}(\beta, \tau)\rangle\langle\psi_{jk,\gamma\gamma}(\beta, \tau)|\}$$
$$= \langle\psi_{jj,\gamma\gamma}(\tau)|\psi_{jk,\gamma\gamma}(\tau)\rangle$$
$$= \langle\psi_{\theta,jj\gamma\gamma}(\tau)|\psi_{\theta,jk\gamma\gamma}(\tau)\rangle \tag{37}$$

which provides the elements of $\mathcal{U}(\tau)$ after obtaining $|\psi_{\gamma,\theta}(\beta, \tau)\rangle$ by integrating eq 29.

5. APPLICATIONS

In this section, we report simulations of electronic population dynamics based on four types of GQMEs. The GQMEs correspond to different subsets of electronic reduced density matrix elements used to describe the underlying dynamics (see Section 3). As described in Section 4, the memory kernels and inhomogeneous terms are calculated from PFIs obtained via the quantum-mechanically exact TT-TFD method as applied to five different realizations of a benchmark spin-boson model Hamiltonian. We also compare the quantum-mechanically exact memory kernels and inhomogeneous terms obtained with TT-TFD inputs to calculations based on an approximate linearized semiclassical (LSC) method.[19]

The reduced electronic density matrix for the spin-boson model, introduced in Section 5.1, consists of four matrix elements: $\{\sigma_{DD}, \sigma_{DA}, \sigma_{AD}, \sigma_{AA}\}$, where $|D\rangle$ and $|A\rangle$ correspond to the *donor* and *acceptor* electronic states, respectively. We

Table 1. Spin-Boson Model and Simulation Parameters

model	model parameters					numerical parameters		
	ϵ	Γ	β	ξ	ω_c	ω_{max}	N_n	Δt
1	1.0	1.0	5.0	0.1	1.0	5	60	1.50083×10^{-3}
2	1.0	1.0	5.0	0.1	2.0	10	60	1.50083×10^{-3}
3	1.0	1.0	5.0	0.1	7.5	36	60	1.50083×10^{-3}
4	1.0	1.0	5.0	0.4	2.0	10	60	7.50415×10^{-4}
6	0.0	1.0	5.0	0.2	2.5	12	60	1.50083×10^{-3}

consider GQMEs for the following four subsets of matrix elements: (1) $\{\sigma_{DD}, \sigma_{DA}, \sigma_{AD}, \sigma_{AA}\}$ (the full density matrix); (2) $\{\sigma_{DD}, \sigma_{AA}\}$ (the populations-only subset); (3) $\{\sigma_{DD}\}$ (the donor single-population subset); and (4) $\{\sigma_{AA}\}$ (the acceptor single-population subset). The TT-TFD-based PFIs, obtained by taking numerical derivatives of the time evolution operator $\mathcal{U}(\tau)$ [see eq 16], are compared to PFIs obtained via an LSC-based method denoted LSCII [also referred to as the LSC initial value representation (LSC-IVR) method[70]]. Reference 44 provides a detailed discussion of the protocols used for calculating PFIs via LSCII.

5.1. Spin-Boson Models. The spin-boson model provides a useful framework for studying molecular systems where the dynamics involves two coupled electronic states. In the simplest form, the electronic coupling is independent of the nuclear coordinates (the so-called "Condon approximation"). The nuclear motion in each electronic state is described by harmonic potential energy surfaces (PESs) with distinct equilibrium energies and equilibrium positions. As such, the spin-boson model has been widely used for describing a wide range of chemical dynamical processes, including charge and energy transfer (e.g., Marcus theory), nonadiabatic dynamics, photochemistry, spin energy relaxation and dephasing, vibrational energy relaxation, and, more recently, polaritonic chemistry where the photonic DOF can be described as harmonic oscillators and therefore grouped with the nuclear DOF.[13−16,71]

The spin-boson Hamiltonian is defined according to eq 1 with $\{\hat{H}_j\}$ and $\{\hat{V}_{jk} \to V_{jk}\}$, which are defined as follows:

$$\hat{H}_1 \equiv \hat{H}_D = \varepsilon + \sum_{k=1}^{N_n} \frac{\hat{P}_k^2}{2} + \frac{1}{2}\omega_k^2 \hat{R}_k^2 - c_k \hat{R}_k$$

$$\hat{H}_2 \equiv \hat{H}_A = -\varepsilon + \sum_{k=1}^{N_n} \frac{\hat{P}_k^2}{2} + \frac{1}{2}\omega_k^2 \hat{R}_k^2 + c_k \hat{R}_k$$

$$V_{12} \equiv V_{DA} = V_{21} \equiv V_{AD} = \Gamma \tag{38}$$

Here, 2ϵ is the energy difference between the donor (D) and acceptor (A) states with nuclear coordinates at equilibrium, and the electronic coupling between donor and acceptor states is defined by the positive constant Γ (the Condon approximation).

The discrete set of N_n frequencies $\{\omega_k\}$ and electron−phonon coupling coefficients $\{c_k\}$ of the nuclear modes are sampled from an Ohmic spectral density with an exponential cutoff:

$$J(\omega) = \frac{\pi}{2}\sum_{k=1}^{N_n} \frac{c_k^2}{\omega_k}\delta(\omega - \omega_k) \xrightarrow{N_n \to \infty} \frac{\pi\hbar}{2}\xi\omega\, e^{-\omega/\omega_c} \tag{39}$$

Here, ξ is the Kondo parameter, which determines the electron−phonon coupling strength, and ω_c is the cutoff frequency, which determines the characteristic vibrational frequency.[43]

The Hamiltonian introduced by eqs 1 and 38 can be rewritten in terms of the harmonic oscillator raising and lowering operators, as follows:

$$\hat{H} = \varepsilon\hat{\sigma}_z + \Gamma\hat{\sigma}_x + \sum_{k=1}^{N_n}\omega_k \hat{a}_k^\dagger \hat{a}_k - \hat{\sigma}_z \frac{c_k}{\sqrt{2\omega_k}}(\hat{a}_k + \hat{a}_k^\dagger) \tag{40}$$

where $\hat{\sigma}_x$ and $\hat{\sigma}_z$ are the x- and z-Pauli matrices. The corresponding rotated double space Hamiltonian $\bar{H}_\theta$ introduced by eq 30 can then be obtained in closed form, as follows:[54,72]

$$\bar{H}_\theta = \varepsilon\hat{\sigma}_z + \Gamma\hat{\sigma}_x + \sum_{k=1}^{N_n}\omega_k(\hat{a}_k^\dagger \hat{a}_k - \tilde{a}_k^\dagger \tilde{a}_k)$$

$$- \frac{\hat{\sigma}_z c_k}{\sqrt{2\omega_k}}((\hat{a}_k + \hat{a}_k^\dagger)\cosh(\theta_k) + (\tilde{a}_k + \tilde{a}_k^\dagger)\sinh(\theta_k)) \tag{41}$$

Using eq 41 in place of the mathematically equivalent eq 30 facilitates the implementation of TT-TFD by avoiding the need to calculate $e^{i\hat{G}}$ and $e^{-i\hat{G}}$ numerically.

The initial state is defined according to eq 2 with the initial electronic state $\hat{\sigma}(0) = |D\rangle\langle D|$ and the initial nuclear state:

$$\hat{\rho}_n(0) = \frac{e^{-\beta(\hat{H}_D + \hat{H}_A)/2}}{\text{Tr}_n\{e^{-\beta(\hat{H}_D + \hat{H}_A)/2}\}} \tag{42}$$

Five different models are analyzed, as defined by the sets of parameters listed in Table 1, corresponding to models 1, 2, 3, 4, and 6 of refs 43, 44, and 19. Model 5 was not included because the reference exact results are known only for short final times, compared to the lifetime of the electronic relaxation dynamics. Models 1−3 correspond to systems with a finite energy bias between the donor and acceptor states (ϵ = 1.0), differing with respect to the value of ω_c. Model 4 corresponds to a biased system (ϵ = 1.0) with a higher Kondo parameter (ξ = 0.4) relative to models 1−3 (ξ = 0.1). Model 6 corresponds to an unbiased system (ϵ = 0.0). All results are obtained using an integration time step $\Delta t = 1.50083 \times 10^{-3}$ Γ^{-1} except for Model 4, which required a smaller time step of $\Delta t = 7.50415 \times 10^{-4}$ Γ^{-1} to fully converge. Quantum-mechanically exact QuAPI results for models 1−4 are taken from ref 39 and results for model 6 are taken from ref 35.

5.2. GQMEs. The following subsections outline four types of GQMEs examined by our simulations, corresponding to the analysis of quantum dynamics for different subsets of electronic reduced density matrix elements.

5.2.1. Full GQME for All Electronic Density Matrix Elements. Here, we consider the GQME where the quantity

of interest includes all four reduced electronic density matrix elements, $\{\sigma_{ab}(t)\} = \{\sigma_{DD}(t), \sigma_{DA}(t), \sigma_{AD}(t), \sigma_{AA}(t)\}$:

$$\frac{d}{dt}\sigma_{jk}(t) = -\frac{i}{\hbar}\sum_{l,m=1}^{N_e=2}\langle\mathcal{L}_{jk,lm}\rangle_n^0\sigma_{lm}(t)$$
$$- \sum_{l,m=1}^{N_e=2}\int_0^t d\tau\,\mathcal{K}_{jk,lm}^{full}(\tau)\sigma_{lm}(t-\tau) \tag{43}$$

where $jk \in \{DD, DA, AD, AA\}$. The memory kernel superoperator $\mathcal{K}^{full}(\tau)$ is represented by an $N_e^2 \times N_e^2 = 4 \times 4$ time-dependent matrix whose matrix elements are obtained by solving the following Volterra equation:

$$\mathcal{K}_{jk,lm}^{full}(\tau) = i\dot{\mathcal{F}}_{jk,lm}(\tau) - \frac{1}{\hbar}\sum_{u,v=1}^{N_e=2}\mathcal{F}_{jk,uv}(\tau)\langle\mathcal{L}_{uv,lm}\rangle_n^0$$
$$+ i\sum_{u,v=1}^{N_e=2}\int_0^\tau d\tau'\,\mathcal{F}_{jk,uv}(\tau-\tau')\mathcal{K}_{uv,lm}^{full}(\tau') \tag{44}$$

where the PFIs $\{\mathcal{F}_{jk,lm}(\tau)\}$ and $\{\dot{\mathcal{F}}_{jk,lm}(\tau)\}$ are introduced by eq 12.

5.2.2. Populations-Only GQME for Diagonal Elements of the Reduced Electronic Density Matrix. Here, we consider the GQME for the quantity of interest that includes only the diagonal matrix elements of the reduced electronic density matrix (i.e., the populations-only GQME), such that $\{\sigma_{ab}(t)\} = \{\sigma_{DD}(t), \sigma_{AA}(t)\}$:

$$\frac{d}{dt}\sigma_{jj}(t) = -\sum_{k=1}^{N_e=2}\int_0^t d\tau\,\mathcal{K}_{jj,kk}^{pop}(\tau)\sigma_{kk}(t-\tau) \tag{45}$$

where $j \in \{D,A\}$. The memory kernel superoperator $\mathcal{K}^{pop}(\tau)$ is represented by an $N_e \times N_e = 2 \times 2$ time-dependent matrix, with individual matrix elements obtained by solving the following Volterra equation:

$$\mathcal{K}_{jj,kk}^{pop}(\tau) = i\dot{\mathcal{F}}_{jj,kk}(\tau) + i\sum_{\lambda=1}^{N_e}\int_0^\tau d\tau'\,\mathcal{F}_{jj,\lambda\lambda}(\tau-\tau')\mathcal{K}_{\lambda\lambda,kk}^{pop}(\tau') \tag{46}$$

where the PFIs $\{\mathcal{F}_{jj,kk}(\tau)\}$ and $\{\dot{\mathcal{F}}_{jj,kk}(\tau)\}$ are introduced by eq 12.

5.2.3. Single-Population Scalar GQMEs for One Diagonal Element of the Reduced Electronic Density Matrix. Finally, we consider the two single-population scalar GQMEs for the case where the subset includes either only the population of the donor state (σ_{DD}) or only the population of the acceptor state (σ_{AA}), such that $\{\sigma_{ab}(t)\} = \{\sigma_{DD}(t)\}$ or $\{\sigma_{ab}(t)\} = \{\sigma_{AA}(t)\}$, respectively:

$$\frac{d}{dt}\sigma_{DD}(t) = -\int_0^t d\tau\,\mathcal{K}_{DD,DD}^{donor}(\tau)\sigma_{DD}(t-\tau) \tag{47}$$

$$\frac{d}{dt}\sigma_{AA}(t) = -\int_0^t d\tau\,\mathcal{K}_{AA,AA}^{acceptor}(\tau)\sigma_{AA}(t-\tau) + I_{AA}^{acceptor}(t) \tag{48}$$

Note that the inhomogeneous term does not vanish in the case where $\{\sigma_{ab}(t)\} = \{\sigma_{AA}(t)\}$. Also note that the memory kernels $\mathcal{K}_{DD,DD}^{donor}(\tau)$ and $\mathcal{K}_{AA,AA}^{acceptor}(\tau)$, as well the inhomogeneous term

$I_{AA}^{acceptor}(t)$, are scalar in this case and can be obtained by solving the following Volterra equations:

$$\mathcal{K}_{DD,DD}^{donor}(\tau) = i\dot{\mathcal{F}}_{DD,DD}(\tau) + i\int_0^\tau d\tau'\,\mathcal{F}_{DD,DD}(\tau-\tau')\mathcal{K}_{DD,DD}^{donor}(\tau') \tag{49}$$

$$\mathcal{K}_{AA,AA}^{acceptor}(\tau) = i\dot{\mathcal{F}}_{AA,AA}(\tau) + i\int_0^\tau d\tau'\,\mathcal{F}_{AA,AA}(\tau-\tau')\mathcal{K}_{AA,AA}^{acceptor}(\tau') \tag{50}$$

$$I_{AA}^{acceptor}(t) = -i\mathcal{F}_{AA,DD}(t) + i\int_0^t d\tau\,\mathcal{F}_{AA,AA}(t-\tau)I_{AA}^{acceptor}(\tau) \tag{51}$$

where the PFIs $\mathcal{F}_{DD,DD}$, $\mathcal{F}_{AA,AA}$, $\dot{\mathcal{F}}_{DD,DD}$, $\dot{\mathcal{F}}_{DD,DD}$, and $\mathcal{F}_{AA,DD}(\tau)$ are defined by eq 12.

5.3. Input Methods. It is important to note that the four types of GQMEs, outlined in the previous subsections, call for the same input of PFIs defined by eq 12. The different types of GQMEs differ only with respect to the specific matrix elements of $\mathcal{F}(\tau)$ and $\dot{\mathcal{F}}(\tau)$ that are required to calculate the memory kernel and inhomogeneous term. For example, calculating the memory kernel for evolving the full set of reduced density matrix elements according to eq 43 requires calculation of all 16 matrix elements of $\mathcal{F}(\tau)$ and $\dot{\mathcal{F}}(\tau)$. In contrast, calculating the memory kernel of the donor single-population GQME (eq 47) requires only a single matrix element of each of the matrices representing $\mathcal{F}(\tau)$ and $\dot{\mathcal{F}}(\tau)$.

The matrix elements of $\mathcal{F}(\tau)$ and $\dot{\mathcal{F}}(\tau)$ can be determined using a wide range of numerically exact or approximate propagation methods. Since the matrix elements of $\mathcal{F}(\tau)$ and $\dot{\mathcal{F}}(\tau)$ are given in terms of two-time correlation functions of the overall system,[19] the only requirement for a propagation method is that it should be able to calculate such quantities, either exactly or approximately.

In this paper, we compare and contrast two input methods: the quantum-mechanically exact TT-TFD method described in Section 4 and the approximate semiclassical LSCII method, previously described in ref 19. The inclusion of the LSCII input method is done for the sake of comparison between the memory kernels and inhomogeneous terms as obtained from an approximate input method with those obtained via an exact input method, with the intent of exploring the main sources of inaccuracy when approximate input methods are used.

For the LSCII method, we calculate $\mathcal{F}_{jk,lm}(\tau)$ and $\dot{\mathcal{F}}_{jk,lm}(\tau)$ directly as described in ref 19. For the TT-TFD method, we calculate the $N_e^2 \times N_e^2$ elements of the time evolution operator of the electronic reduced density matrix $\mathcal{U}(\tau)$ introduced by eq 16. Then, $\mathcal{F}_{jk,lm}(\tau)$ and $\dot{\mathcal{F}}_{jk,lm}(\tau)$ are obtained from numerical derivatives according to eq 17. For the results given in this paper, the numerical derivatives were calculated using the second-order finite central difference method available in the NumPy Python library. The same time step is used for both LSCII and TT-TFD (see Table 1) and 10^6 trajectories were used for LSCII.

Once the PFIs have been obtained with either TT-TFD or LSCII propagation, the memory kernels and inhomogeneous terms of the GQMEs are calculated via an iterative algorithm that solves the corresponding Volterra equation (see eqs 44, 46, 49, 50, and 51).[19,43] The different types of GQMEs (see eqs 43, 45, 47, and 48) are then solved numerically for the
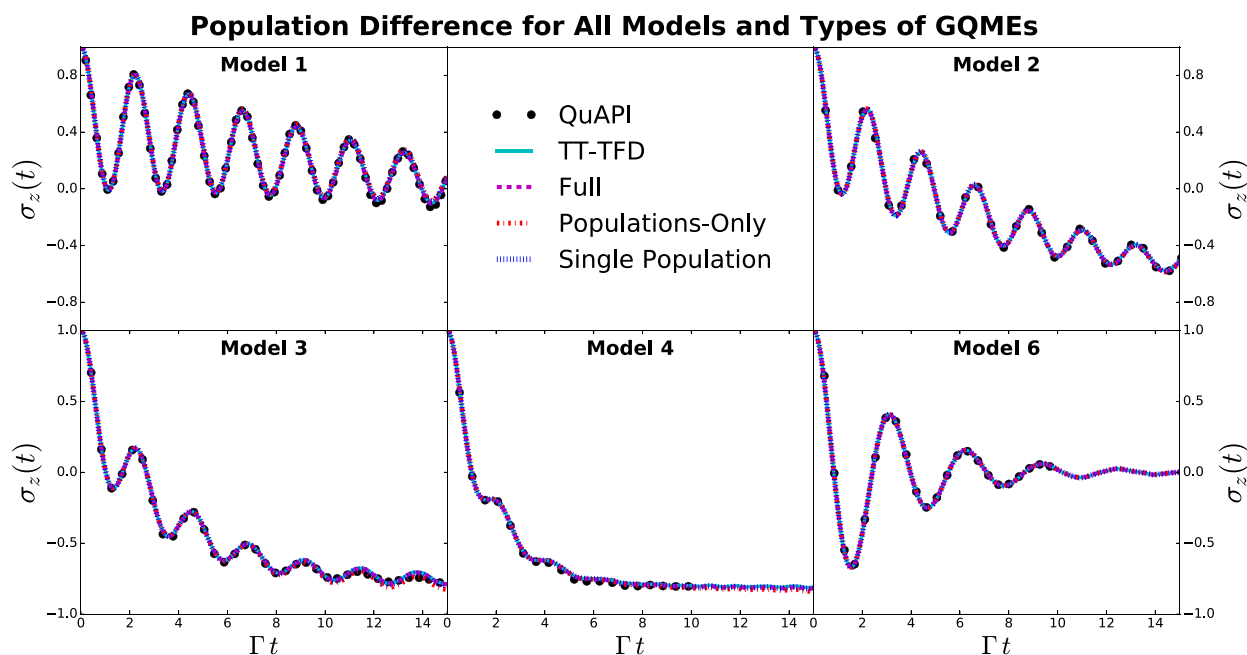
Figure 1. Electronic population difference $\sigma_z(t) = \sigma_{DD}(t) - \sigma_{AA}(t)$, as a function of time for all models in Table 1. Shown are exact QuAPI results (black circles) and results obtained based on the following: direct application of TT-TFD (solid cyan line); the full density matrix GQME of the form of eq 43 with TT-TFD-based PFIs (dashed magenta line); a populations-only GQME of the form of eq 45 with TT-TFD-based PFIs (dashed-dotted red line); and a combination of the two single-population scalar GQMEs of the form of eqs 47 and 48 for $\sigma_{DD}(t)$ and $\sigma_{AA}(t)$, respectively, with TT-TFD-based PFIs (dotted blue line).

electronic density matrix elements via a Runge−Kutta fourth-order (RK4) algorithm.

5.4. Results. Figure 1 compares the time-dependent $\sigma_z(t) = \sigma_{DD}(t) - \sigma_{AA}(t)$, showing the differences of electronic populations for the five realizations of the spin-boson model outlined in Section 5.1 (see Table 1). These results are obtained by using the four different types of GQMEs outlined in Section 5.2, with PFIs computed with the TT-TFD method as described in Section 4. These results provide a clear demonstration of the rather remarkable fact that *all four GQMEs correspond to exact equations of motion for the electronic populations* and thereby reproduce the same exact population dynamics when a quantum-mechanically exact input method like TT-TFD is used, even though they are quite different in form and dimensionality.

Next, we focus on model 4 for a more-detailed analysis, with the analogous analysis for the other models provided in the SI. Figure 2 compares the population relaxation dynamics for model 4 (see Table 1), obtained with different types of GQMEs and memory kernels calculated by TT-TFD and LSCII input methods. The population relaxation dynamics generated via the LSCII-based populations-only GQME is in excellent agreement with the exact results. At the same time, the population relaxation dynamics generated via the LSCII-based single-population GQMEs is inaccurate. The origin of this discrepancy can be traced back to the fact that the LSCII-based single-population GQMEs do not conserve population (i.e., $\sigma_{DD}(t) + \sigma_{AA}(t) \neq 1$).

Figures 3 and 4 show the real and imaginary parts of the TT-TFD full memory kernels for model 4, as compared to the real and imaginary parts of the LSCII memory kernels for the same model.[19] Each figure includes 16 graphs, corresponding to the elements of the 4×4 memory kernel matrix. Since the memory kernel for the full electronic density matrix GQME is represented by a 4×4 matrix, it has elements in all 16 graphs

in Figures 3 and 4. In contrast, the memory kernel of the populations-only GQME is represented by a 2×2 matrix (see eqs 45 and 46). The real and imaginary parts of the four elements of the populations-only memory kernel are shown in Figures 5 and 6. The memory kernels of the two single-population GQMEs are scalar (see eqs 47−50) and their real and imaginary parts are each therefore shown in one graph (the top left corner for the donor single-population GQME and the bottom right corner for the acceptor single-population GQME in Figures 5 and 6, respectively).

We start the analysis with the memory kernel in the case of the GQME for the full electronic density matrix, $\mathcal{K}^{full}(\tau)$. In this case, it can be shown analytically that the quantum-mechanically exact memory kernel matrix elements, whose real and imaginary values are given in the top and bottom rows of Figures 3 and 4, respectively, should vanish [i.e., $\mathcal{K}^{full}_{DDDD} = \mathcal{K}^{full}_{DDDA}(\tau) = \mathcal{K}^{full}_{DDAD}(\tau) = \mathcal{K}^{full}_{DDAA}(\tau) = \mathcal{K}^{full}_{AADD}(\tau) = \mathcal{K}^{full}_{AADA}(\tau) = \mathcal{K}^{full}_{AAAD}(\tau) = \mathcal{K}^{full}_{AAAA}(\tau) = 0$]. This can be seen by casting the memory kernel in the following alternative form that was derived in ref 43:

$$\mathcal{K}^{full}_{ab,cd}(\tau) = \frac{1}{\hbar^2} \text{Tr}\{|b\rangle\langle a|\mathcal{L}_{zero} e^{-iQ\mathcal{L}\tau/\hbar} Q\mathcal{L}_{zero}\hat{\rho}_n(0)|c\rangle\langle d|\}$$

(52)

where $\mathcal{L}_{zero}(\cdot) = \left[\sum_{j=1}^{N_e} \hat{H}_j|j\rangle\langle j|, \cdot\right] = [\hat{H}_{zero}, \cdot]$. For any system satisfying the Condon approximation, $\hat{V}_{jk} \to V_{jk}$ (such as the spin-boson model under consideration in this paper), eq 52 is equivalent to eq 44, with the proof given in Appendix A of ref 43. The fact that

$$|a\rangle\langle a|\mathcal{L}_{zero} = \left[|a\rangle\langle a|, \sum_{j=1}^{N_e} \hat{H}_j|j\rangle\langle j|\right] = \delta_{a,j}|a\rangle\langle a|\hat{H}_a - \delta_{a,j}\hat{H}_a|a\rangle\langle a| = 0$$

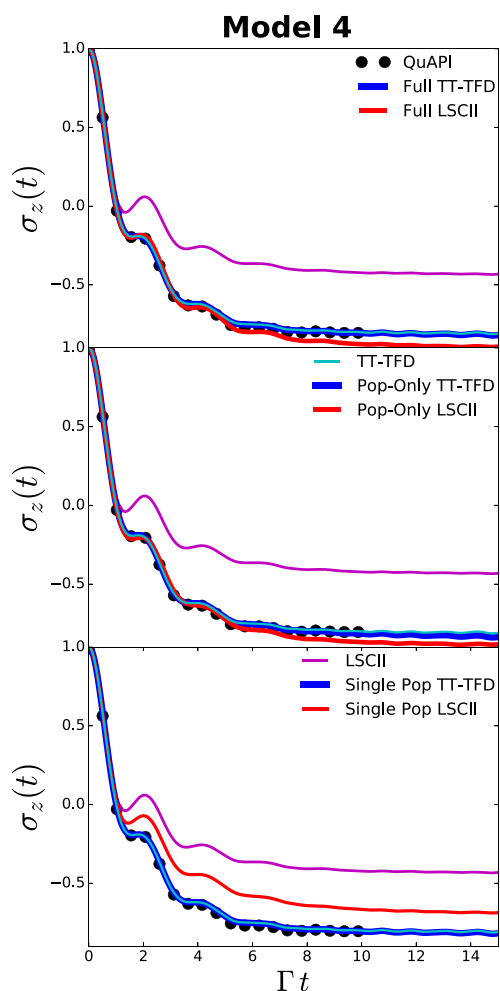**Figure 2.** Electronic population difference $\sigma_z(t) = \sigma_{DD}(t) - \sigma_{AA}(t)$, as a function of time for model 4 in Table 1. Shown are exact QuAPI (black circles) and TT-TFD (cyan lines) results; LSCII result (purple lines); and full GQME (upper plot), populations-only GQME (middle plot) and combination of two single-population scalar GQMEs (lower plot) results obtained with TT-TFD-based PFIs (blue line) and LSCII-based PFIs (red line).

then implies that $\mathcal{K}_{aa,cd}^{full}(\tau) = 0$.

While the real and imaginary parts of the TT-TFD-based memory kernel matrix elements in the first and fourth rows of Figures 3 and 4 are nonzero, they are much smaller than the matrix elements in the second and third rows. This behavior is consistent with the above-mentioned analytical result, with the small nonzero values attributable to numerical noise.

Note that $\langle \mathcal{L} \rangle_n^0$ can also couple density matrix elements (see eq 43). For the spin-boson model under consideration here,

$$\langle \mathcal{L} \rangle_n^0 = \begin{pmatrix} 0 & -\Gamma & \Gamma & 0 \\ -\Gamma & 2\varepsilon & 0 & \Gamma \\ \Gamma & 0 & -2\varepsilon & -\Gamma \\ 0 & \Gamma & -\Gamma & 0 \end{pmatrix} \tag{53}$$

Importantly, while the DDAD, DDDA, AADA, and AAAD elements of $\langle \mathcal{L} \rangle_n^0$ are nonzero, the DDAA, DDDD, AADD, and AAAA elements of $\langle \mathcal{L} \rangle_n^0$ vanish. This implies that, in the case of the full GQME for the spin-boson model, population transfer from the donor (σ_{DD}) to the acceptor (σ_{AA}) corresponds to a

two-step process. It starts with population-to-coherence transfer induced by coupling between σ_{DD} and σ_{DA} or σ_{AD} via the Liouvillian term and then proceeds to coherence-to-population transfer induced by coupling between σ_{DA} or σ_{AD} and σ_{AA} via the Liouvillian term and the memory kernel term.

Comparison of the eight matrix elements of the memory kernel that couple populations and coherences, namely, $\{\mathcal{K}_{DDDA}^{full}, \mathcal{K}_{DDAD}^{full}, \mathcal{K}_{DADD}^{full}, \mathcal{K}_{DAAA}^{full}, \mathcal{K}_{ADDD}^{full}, \mathcal{K}_{ADAA}^{full}, \mathcal{K}_{AADA}^{full}, \mathcal{K}_{AAAD}^{full}\}$, reveals several trends:

- The agreement between TT-TFD and LSCII is significantly better for the matrix elements $\{\mathcal{K}_{DADD}^{full}, \mathcal{K}_{DAAA}^{full}, \mathcal{K}_{ADDD}^{full}, \mathcal{K}_{ADAA}^{full}\}$ than for the matrix elements $\{\mathcal{K}_{DDDA}^{full}, \mathcal{K}_{DDAD}^{full}, \mathcal{K}_{AADA}^{full}, \mathcal{K}_{AAAD}^{full}\}$. At the same time, the four matrix elements $\{\mathcal{K}_{DDDA}^{full}, \mathcal{K}_{DDAD}^{full}, \mathcal{K}_{AADA}^{full}, \mathcal{K}_{AAAD}^{full}\}$ are significantly smaller than the remaining four matrix elements $\{\mathcal{K}_{DADD}^{full}, \mathcal{K}_{DAAA}^{full}, \mathcal{K}_{ADDD}^{full}, \mathcal{K}_{ADAA}^{full}\}$. Thus, LSCII appears to capture the larger-amplitude matrix elements better than the smaller ones. Given the expectation that the larger-amplitude matrix elements would play a more significant role in the dynamics, this observation is consistent with the relative accuracy of the LSCII-based GQME.

- Whereas the real parts of the larger matrix elements $\{\mathcal{K}_{DADD}^{full}, \mathcal{K}_{DAAA}^{full}, \mathcal{K}_{ADDD}^{full}, \mathcal{K}_{ADAA}^{full}\}$ are seen to be relatively short-lived (compared to the population relaxation time scale, see Figure 1) and exhibit a monotonic decay, the imaginary parts are seen to be oscillatory and do not appear to decay. Note that the oscillatory behavior of the imaginary parts obtained via LSCII is damped, compared to exact results obtained via TT-TFD. The observed damping is likely a manifestation of the quasiclassical nature of LSCII, which limits its ability to accurately capture coherent quantum dynamics. Since one expects the real parts to dominate population relaxation rates, the relative accuracy of the LSCII-based GQME can be attributed to the ability of LSCII to capture the real parts rather well.

Examination of the remaining nonvanishing matrix elements, $\{\mathcal{K}_{DADA}^{full}, \mathcal{K}_{DAAD}^{full}, \mathcal{K}_{ADDA}^{full}, \mathcal{K}_{ADAD}^{full}\}$, reveals the following trends:

- The real parts of $\mathcal{K}_{DADA}^{full}$ and $\mathcal{K}_{ADAD}^{full}$ are significantly larger and less oscillatory than the real parts of $\mathcal{K}_{DAAD}^{full}$ and $\mathcal{K}_{ADDA}^{full}$. This implies that the dynamics of the coherences σ_{DA} and σ_{AD} is dominated by dephasing (with rates dictated by $\mathcal{K}_{DADA}^{full}$ and $\mathcal{K}_{ADAD}^{full}$) and that coherence-to-coherence transfer (with rates dictated by $\mathcal{K}_{DAAD}^{full}$ and $\mathcal{K}_{ADDA}^{full}$) is significantly slower than dephasing. This is consistent with the secular approximation (also called the rotating wave approximation), which is often invoked to eliminate coherence transfer terms from perturbative quantum master equations.[73]

- LSCII appears to capture the real parts of $\{\mathcal{K}_{DADA}^{full}, \mathcal{K}_{ADAD}^{full}, \mathcal{K}_{DAAD}^{full}, \mathcal{K}_{ADDA}^{full}\}$ rather accurately. LSCII also appears to be less accurate when it comes to capturing the corresponding imaginary parts, with the inaccuracy manifested by an overdamping of the oscillatory behavior. This behavior is similar to that
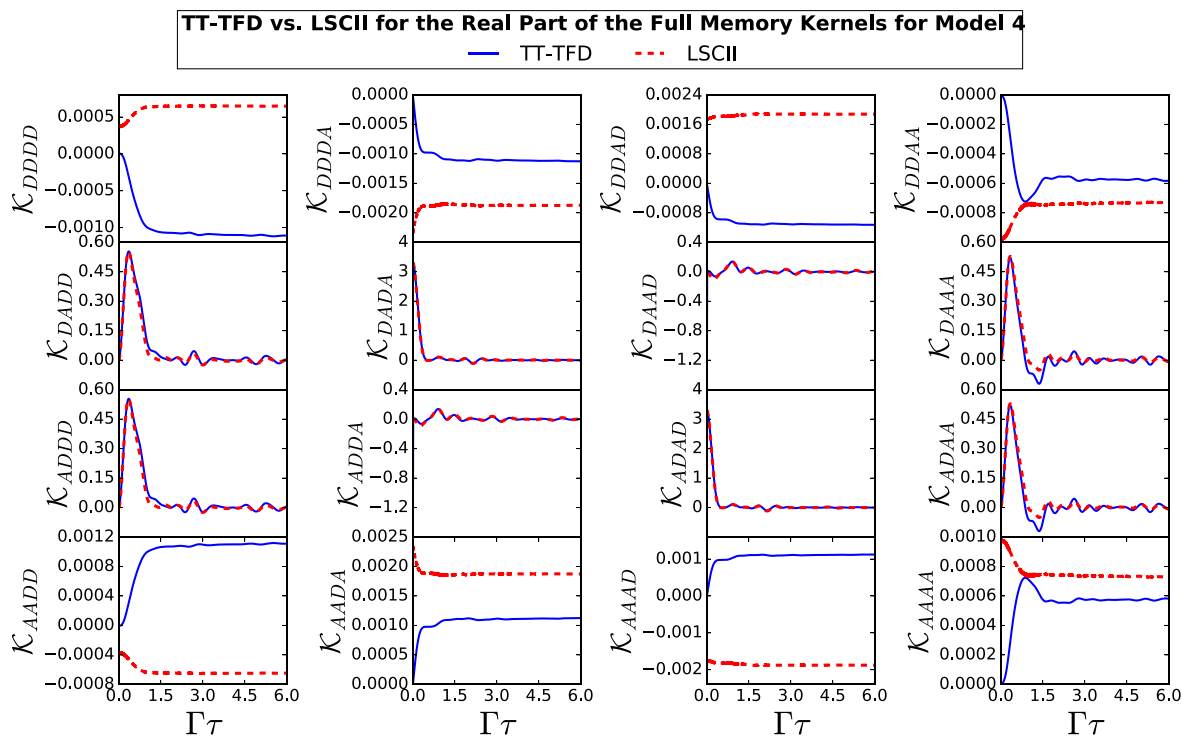
Figure 3. Real parts of the matrix elements of the memory kernel of the GQME for the full electronic density matrix $[\mathcal{K}^{\text{full}}(\tau)$ in eq 44] for model 4, as obtained from TT-TFD-based PFIs (solid blue lines) and LSCII-based PFIs (dashed red lines). Similar graphs for the other four models are provided in the SI.

Figure 4. Imaginary parts of the matrix elements of the memory kernel of the GQME for the full electronic density matrix $[\mathcal{K}^{\text{full}}(\tau)$ in eq 44] for model 4, as obtained from TT-TFD-based PFIs (solid blue lines) and LSCII-based PFIs (dashed red lines). Similar graphs for the other four models are provided in the SI.
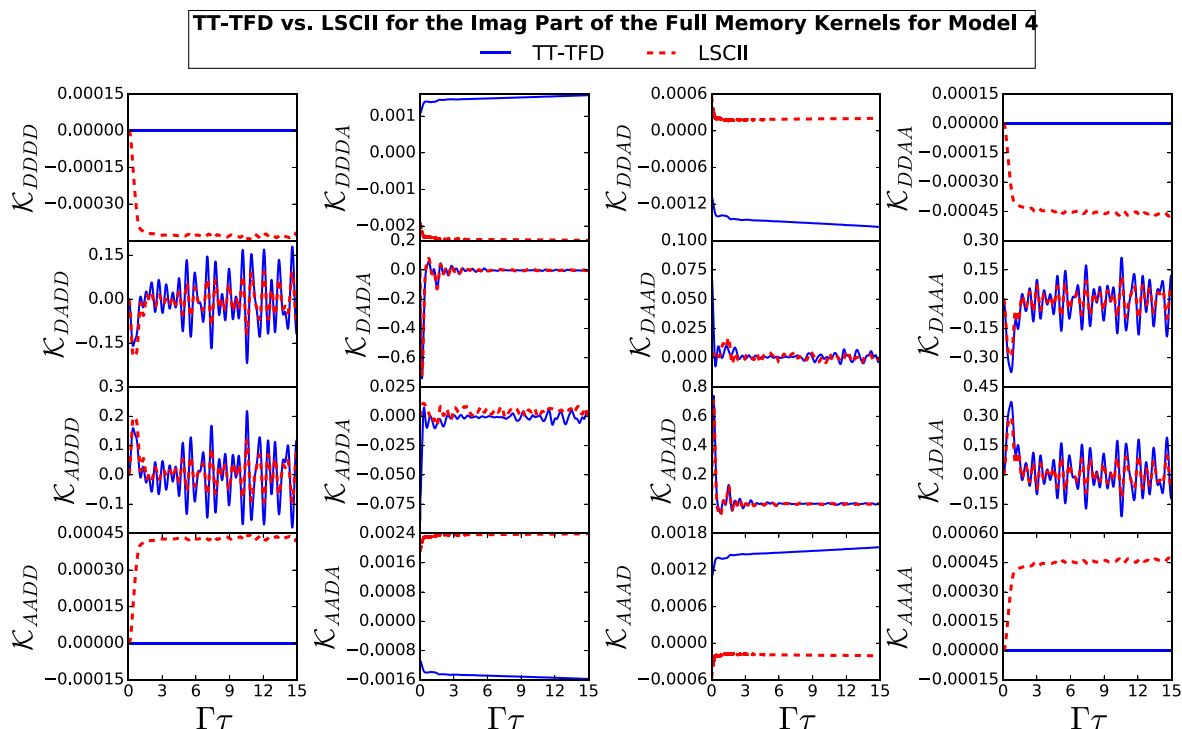
noted above, regarding other matrix elements, and is consistent with the quasiclassical nature of the approximations on which LSCII is based.

Given that population transfer is mediated by the coherences in the case of the full density matrix GQME, the accuracy of the real parts of the LSCII-based $\{\mathcal{K}^{\text{full}}_{\text{DADA}}, \mathcal{K}^{\text{full}}_{\text{DAAD}}, \mathcal{K}^{\text{full}}_{\text{ADDA}}, \mathcal{K}^{\text{full}}_{\text{ADAD}}\}$ likely plays an important
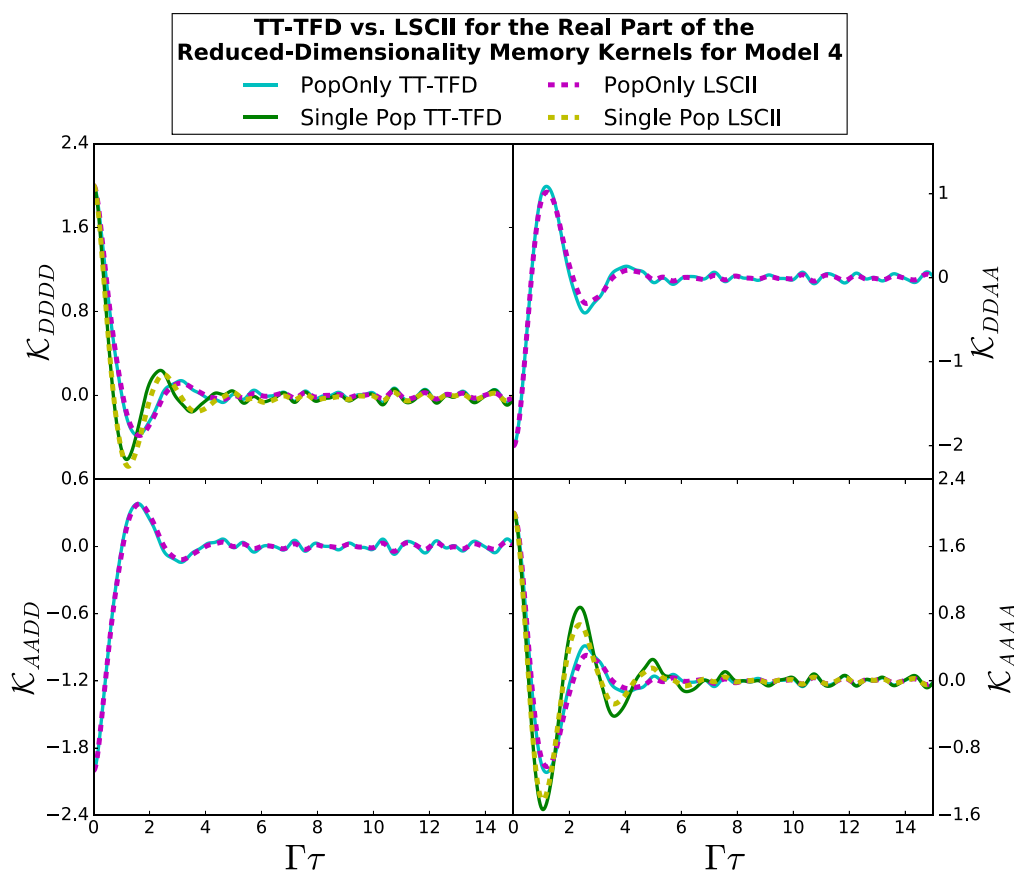
Figure 5. Real parts of the matrix elements of the memory kernels for the populations-only and single-population GQMEs for model 4, as obtained from TT-TFD-based PFIs and LSCII-based PFIs. Shown are the matrix elements of three different memory kernels: (1) The memory kernel of the populations-only GQME [$\mathcal{K}^{\text{pop}}(\tau)$ in eq 46], which has four elements (DDDD, DDAA, AADD, and AAAA) and is depicted with solid cyan lines for the results from TT-TFD-based PFIs and dashed magenta lines for the results from LSCII-based PFIs; (2) and (3) The single-element memory kernels of the scalar single-population GQMEs [$\mathcal{K}_{\text{DD,DD}}^{\text{donor}}(\tau)$ and $\mathcal{K}_{\text{AA,AA}}^{\text{acceptor}}(\tau)$, in eqs 49 and 50, respectively], which are depicted in the DDDD and AAAA panels, respectively, with solid green lines for the results from TT-TFD-based PFIs and dashed yellow lines for the results from LSCII-based PFIs. Graphs with the results for the other four models are provided in the SI.

role in the ability of the LSCII-based GQME to accurately predict the population relaxation dynamics (see Figure 2).

Next, we consider the memory kernel in the case of the GQME for the electronic populations, $\mathcal{K}^{\text{pop}}(\tau)$ (see eqs 45 and 46). In this case, the memory kernel is given in terms of a 2 × 2 matrix that consists of the memory kernel elements in Figures 5 and 6: {$\mathcal{K}_{\text{DDDD}}^{\text{pop}}$, $\mathcal{K}_{\text{DDAA}}^{\text{pop}}$, $\mathcal{K}_{\text{AADD}}^{\text{pop}}$, $\mathcal{K}_{\text{AAAA}}^{\text{pop}}$}. The dimensionality of $\mathcal{K}^{\text{pop}}(\tau)$ should be contrasted with the $\mathcal{K}^{\text{full}}(\tau)$, for which the same four matrix elements vanish. Since the coherences have been projected out for this GQME, the memory kernel gives rise to direct coupling between populations, as opposed to population transfer being mediated by the coherences. As a result, donor-to-acceptor population transfer corresponds to a one-step process.

Comparison of the TT-TFD-based and LSCII-based real and imaginary parts of {$\mathcal{K}_{\text{DDDD}}^{\text{pop}}$, $\mathcal{K}_{\text{DDAA}}^{\text{pop}}$, $\mathcal{K}_{\text{AADD}}^{\text{pop}}$, $\mathcal{K}_{\text{AAAA}}^{\text{pop}}$} reveals the following notable trends:

- The real parts of those four memory kernel matrix elements are comparable in size and exhibit a damped oscillatory behavior that is longer-lived than the nonvanishing matrix elements of $\mathcal{K}^{\text{full}}(\tau)$. This behavior is consistent with previous studies[19,38] and can be traced back to the fact that, in this case, the memory kernel also

must account for the impact of the projected-out electronic coherences on the electronic populations.

- LSCII is highly accurate when it comes to reproducing the real parts of the exact TT-TFD-based {$\mathcal{K}_{\text{DDDD}}^{\text{pop}}$, $\mathcal{K}_{\text{DDAA}}^{\text{pop}}$, $\mathcal{K}_{\text{AADD}}^{\text{pop}}$, $\mathcal{K}_{\text{AAAA}}^{\text{pop}}$}. Given that the real parts of the $\mathcal{K}^{\text{pop}}(\tau)$ matrix elements dominate the population transfer kinetics, this observation is consistent with the previously made observation that the LSCII-based populations-only GQME can reproduce the population relaxation rather well.[19]

- Whereas the imaginary parts of {$\mathcal{K}_{\text{DDDD}}^{\text{pop}}$, $\mathcal{K}_{\text{DDAA}}^{\text{pop}}$, $\mathcal{K}_{\text{AADD}}^{\text{pop}}$, $\mathcal{K}_{\text{AAAA}}^{\text{pop}}$} computed with TT-TFD vanish, the corresponding LSCII values do not. The discrepancy is due to errors in the calculation of $\dot{\mathcal{F}}_{jj,mm}(\tau)$ elements with LSCII, which generates a small real part for the $\dot{\mathcal{F}}_{jj,mm}(\tau)$ elements, which should be purely imaginary. However, the failure of LSCII to accurately predict the imaginary parts does not appear to impact the accuracy of the population transfer kinetics, since the imaginary parts are 2 orders of magnitude smaller than the real parts.

Finally, we consider the scalar memory kernels in the donor and acceptor single-population GQMEs, $\mathcal{K}_{\text{DDDD}}^{\text{donor}}(\tau)$ and
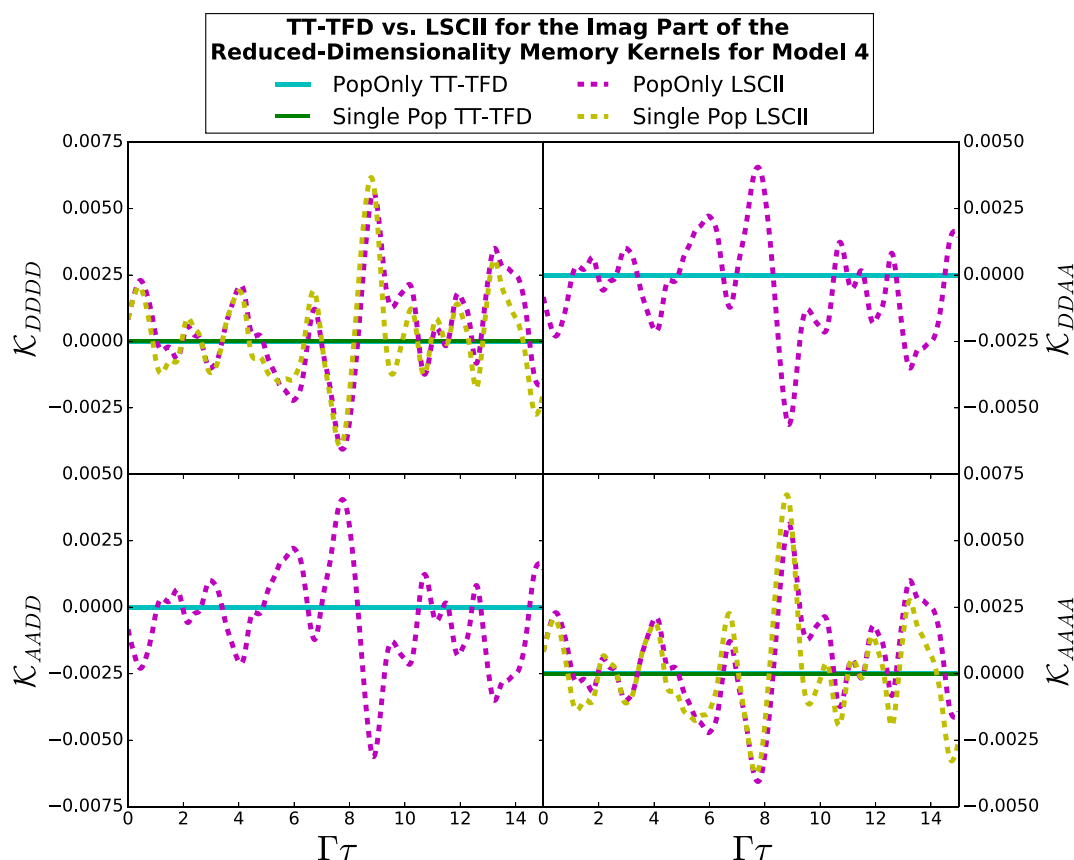
Figure 6. Imaginary parts of the matrix elements of the memory kernels for the populations-only and single-population GQMEs for model 4, as obtained from TT-TFD-based PFIs and LSCII-based PFIs. Shown are the matrix elements of three different memory kernels: (1) The memory kernel of the populations-only GQME [$\mathcal{K}^{pop}(\tau)$ in eq 46], which has four elements (DDDD, DDAA, AADD, and AAAA) and is depicted with solid cyan lines for the results from TT-TFD-based PFIs and dashed magenta lines for the results from LSCII-based PFIs; (2 and 3) the single-element memory kernels of the scalar single-population GQMEs [$\mathcal{K}^{donor}_{DD,DD}(\tau)$ and $\mathcal{K}^{acceptor}_{AA,AA}(\tau)$, in eqs 49 and 50, respectively], which are depicted in the DDDD and AAAA panels, respectively, with solid green lines for the results from TT-TFD-based PFIs and dashed yellow lines for the results from LSCII-based PFIs. Graphs with the results for the other four models are provided in the SI.

$\mathcal{K}^{acceptor}_{AAAA}(\tau)$, respectively (see eqs 47−50). In this case, $\mathcal{K}^{donor}_{DDDD}(\tau)$ is given by the top-left corner element and $\mathcal{K}^{acceptor}_{AAAA}(\tau)$ is given by the bottom-right corner element in Figures 5 and 6. Comparison of the real and imaginary parts of $\mathcal{K}^{donor}_{DDDD}(\tau)$ and $\mathcal{K}^{acceptor}_{AAAA}(\tau)$ computed with TT-TFD and LSCII reveals the following notable trends:

- The real parts of $\mathcal{K}^{donor}_{DDDD}(\tau)$ and $\mathcal{K}^{acceptor}_{AAAA}(\tau)$ are comparable in size and exhibit a damped oscillatory behavior with a lifetime similar to that of the populations-only memory kernel elements.

- LSCII is highly accurate for reproducing the real part of the exact TT-TFD-based $\mathcal{K}^{donor}_{DDDD}(\tau)$. The accuracy is somewhat lower for reproducing the real part of $\mathcal{K}^{acceptor}_{AAAA}(\tau)$.

- While the imaginary parts of $\mathcal{K}^{donor}_{DDDD}(\tau)$ and $\mathcal{K}^{acceptor}_{AAAA}(\tau)$ computed with TT-TFD vanish, the corresponding LSCII values do not. However, the failure of LSCII to accurately predict the imaginary parts does not appear to impact the accuracy of the population transfer kinetics, since the imaginary parts are 2 orders of magnitude smaller than the real parts.

In Figure 7, we show the real part of the inhomogeneous term of the acceptor single-population GQME, $\hat{I}_{AA}(t)$, which is the only GQME with an inhomogeneous term considered in

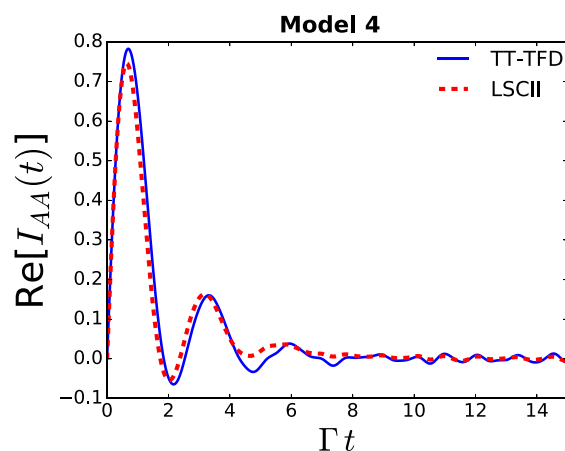**Figure 7.** Real part of $\hat{I}_{AA}(\tau)$ (see eq 51) for model 4, as obtained from TT-TFD-based PFIs (solid blue lines) and LSCII-based PFIs (dashed red lines). Similar graphs for the other four models are included in the SI.
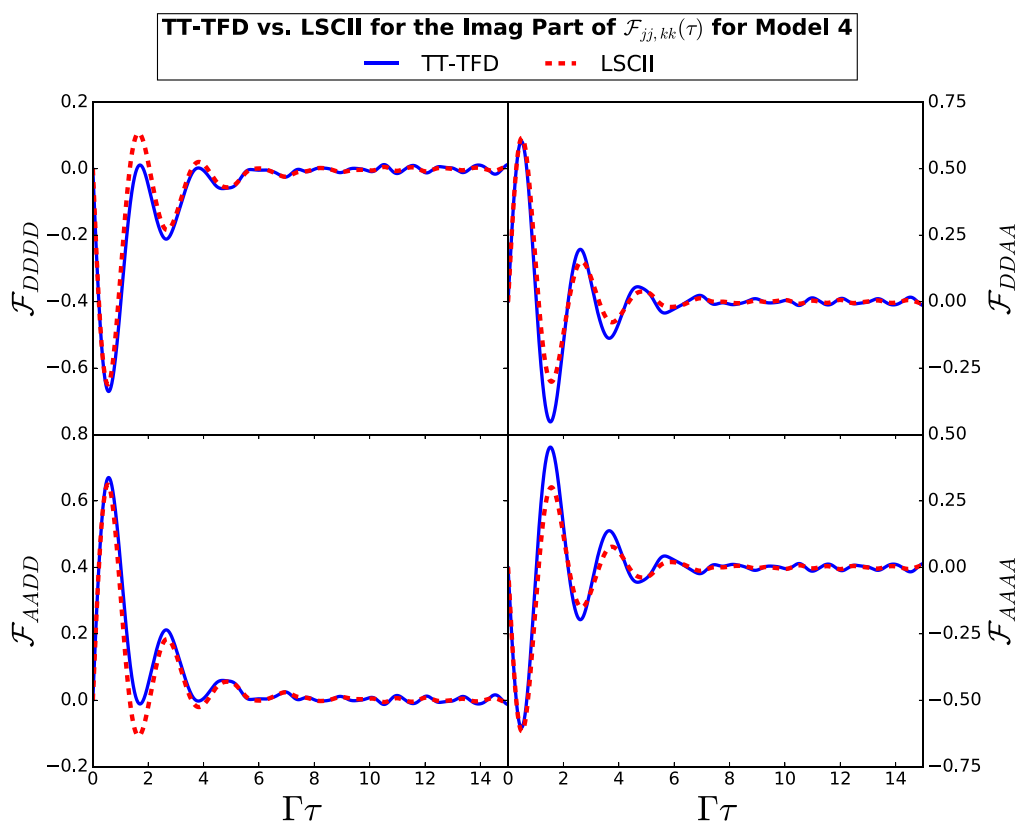
Figure 8. Imaginary parts of the DDDD, DDAA, AADD, and AAAA matrix elements of $\mathcal{F}(\tau)$ [see eq 12] for model 4, as obtained via TT-TFD (solid blue lines) and LSCII (dashed red lines). Similar graphs for the other four models are included in the SI.

this paper. The imaginary component is not shown, because it is zero for the results from both TT-TFD-based and LSCII-based PFIs. In the figure, we see that the inhomogeneous term from LSCII-based PFIs is slightly overdamped, compared to the inhomogeneous term from the TT-TFD-based PFIs.

To understand the origin of the inaccuracies in the LSCII-based single-population GQMEs relative to the populations-only GQME, we note that any such inaccuracies must come from inaccuracies in $\mathcal{F}(\tau)$ and $\dot{\mathcal{F}}(\tau)$, as the subsequent steps of the GQME approach are exact. To this end, in Figure 8, we show the imaginary components of the matrix elements of $\mathcal{F}(\tau)$, in Figures 9 and 10, the real and imaginary components of the matrix elements of $\dot{\mathcal{F}}(\tau)$ that are used as PFIs to obtain the memory kernels for the single-population and populations-only GQMEs. The real parts of $\mathcal{F}(\tau)$ are not shown, because they are zero for these elements from both LSCII and TT-TFD. These figures clearly show that, although the LSCII-based $\mathcal{F}(\tau)$ and $\dot{\mathcal{F}}(\tau)$ matrix elements can be rather accurate, there are significant deviations from the exact ones. The deviations are the origin of any inaccuracies in the memory kernels obtained from them.

We now show that, although the errors in $\mathcal{F}(\tau)$ affect the memory kernels of both single-population and populations-only GQMEs, the effect is weaker on the latter because of error cancellation. To see this difference in effect, we note that $\mathcal{K}_{\mathrm{DD,DD}}^{\mathrm{pop}}(\tau)$ and $\mathcal{K}_{\mathrm{DD,DD}}^{\mathrm{donor}}(\tau)$ are obtained from the PFIs via eq 46 and 49:

$$\mathcal{K}_{\mathrm{DD,DD}}^{\mathrm{pop}}(\tau) = i\dot{\mathcal{F}}_{\mathrm{DD,DD}}(\tau) + i\int_0^\tau \mathrm{d}\tau\,'[\mathcal{F}_{\mathrm{DD,DD}}(\tau - \tau')\mathcal{K}_{\mathrm{DD,DD}}^{\mathrm{pop}}(\tau')$$
$$+ \mathcal{F}_{\mathrm{DD,AA}}(\tau - \tau')\mathcal{K}_{\mathrm{AA,DD}}^{\mathrm{pop}}(\tau')] \quad (54)$$

$$\mathcal{K}_{\mathrm{DD,DD}}^{\mathrm{donor}}(\tau) = i\dot{\mathcal{F}}_{\mathrm{DD,DD}}(\tau)$$
$$+ i\int_0^\tau \mathrm{d}\tau'\,\mathcal{F}_{\mathrm{DD,DD}}(\tau - \tau')\mathcal{K}_{\mathrm{DD,DD}}^{\mathrm{donor}}(\tau')$$
$$(55)$$

Importantly, the integrand on the right-hand side of eq 54 gives rise to inherent error cancellation, since $\mathcal{K}_{\mathrm{DD,DD}}^{\mathrm{pop}}(\tau)$ and $\mathcal{K}_{\mathrm{AA,DD}}^{\mathrm{pop}}(\tau)$ are of opposite sign, which causes the errors in $\mathcal{F}(\tau)$ to cancel when they are correlated. Such correlation is observed for all of the models that we studied, e.g., in Figure 8, most evidently at $t = 1.9\ \Gamma$, the approximate method significantly overestimated both $\mathcal{F}_{\mathrm{DD,DD}}(\tau)$ and $\mathcal{F}_{\mathrm{DD,AA}}(\tau)$. On the other hand, eq 55 does not allow for such error cancellation, thereby making the single-population GQMEs less accurate than the populations-only GQME.

5.5. Computational Cost. In this section, we examine the scaling of the computational cost of the GQME approach with TT-TFD as the input method, with respect to GQME type.

We begin by considering the time step used to calculate the TT-TFD-based PFIs to obtain the converged memory kernel and the inhomogeneous term. In contrast to LSCII, which required a similar time step for all GQMEs,[19] the time step needed for convergence is found to decrease with decreasing dimensionality. More specifically, although the results shown above are all for a time step of $\Delta t = 0.00150083\ \Gamma^{-1}$ (except for model 4, see Table 1), the time step needed for convergence for the full density matrix GQME is in the
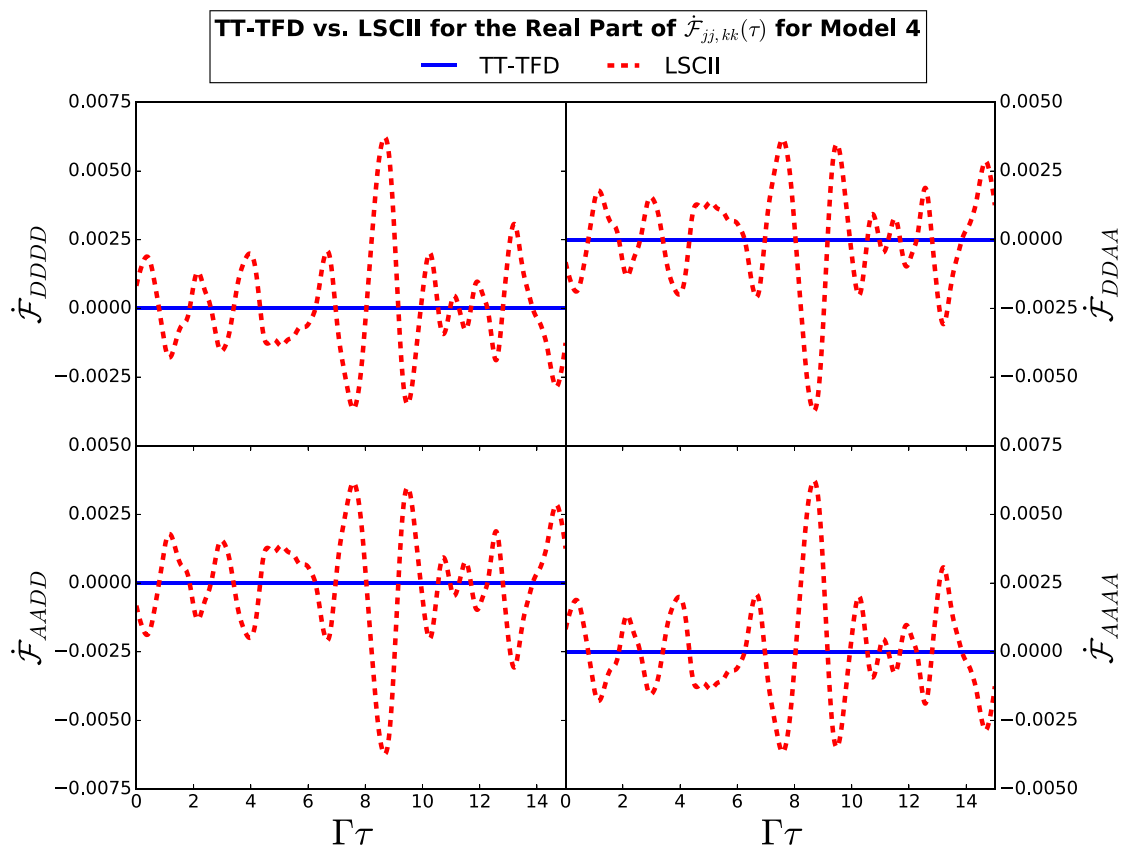
Figure 9. Real parts of the DDDD, DDAA, AADD, and AAAA matrix elements of $\dot{\mathcal{F}}(\tau)$ (see eq 12) for model 4, as obtained via TT-TFD (solid blue lines) and LSCII (dashed red lines). Similar graphs for the other four models are included in the SI.

range of $\Delta t = 0.00300166-0.00450249\ \Gamma^{-1}$, in contrast to the time step of $\Delta t = 0.00150083\ \Gamma^{-1}$ that was required in the case of the populations-only and single-population GQMEs (except for the populations-only GQME of model 4, which required a time step of $\Delta t = 0.000750415\ \Gamma^{-1}$).

In ref 19, we noted that the direct calculation of $\dot{\mathcal{F}}_{jk,lm}(\tau)$ given in eq 12 required calculation of the dynamics for more electronic initial conditions than only $|j\rangle\langle k|$ due to terms involving off-diagonal components of the Hamiltonian in the initial state. However, although direct calculation of $\dot{\mathcal{F}}_{jk,lm}(\tau)$ is necessary when using approximate input methods, when using exact input methods, we can obtain $\dot{\mathcal{F}}_{jk,lm}(\tau)$ from $\mathcal{U}_{jk,lm}(\tau)$ as described in eq 17. Therefore, we only need to calculate the dynamics for the initial electronic state $|j\rangle\langle k|$ to obtain $\mathcal{U}_{jk,lm}(\tau)$ and, subsequently, $\mathcal{F}_{jk,lm}(\tau)$ and $\dot{\mathcal{F}}_{jk,lm}(\tau)$ through eq 17. As a result, there is a significant reduction in the number of initial electronic states necessary to calculate the PFIs needed for the reduced-dimensionality GQMEs compared to the full GQME. More specifically, although the full GQME approach requires simulating the dynamics for four initial electronic states in the case of a two-state system, the populations-only GQME requires only two initial electronic states, the acceptor single-population GQME approach requires two initial electronic states (with one of them due to the inhomogeneous term), and the donor single-population GQME requires only one initial electronic state. Thus, reduced-dimensionality GQMEs significantly enhance computational efficiency with regard to the number of initial states

that must be simulated when exact input methods such as TT-TFD are used.

Next, we consider the cost of obtaining the memory kernels from the PFIs. The computational complexity of each iteration in the Volterra algorithm for the memory kernel is expected to be $O(N_{mat}^3)$, where N_{mat} is the number of matrix elements in a row of the memory kernel matrix (e.g., $N_{mat} = N_e^2$ for the full GQME, $N_{mat} = N_e$ for the populations-only GQME, and $N_{mat} = 1$ for the single-population GQMEs). This is true regardless of the input method used and, therefore, the cost of each iteration of the Volterra algorithm increases dramatically with memory kernel size. The computational complexity of each iteration in the Volterra algorithm for the inhomogeneous term scales more favorably at $O(N_{mat}^2)$ but may still become restrictive with increasing dimensionality. However, note that the inhomogeneous term often is not needed for the larger-dimensional full and populations-only GQME approaches.

The number of iterations required for the iterative Volterra algorithm for the memory kernel to converge is also rather sensitive to the type of GQME and the dimensionality of the electronic observable of interest. More specifically, whereas 2 iterations are required for calculating the single-population memory kernels and 2−3 iterations are needed in the case of the populations-only memory kernel for all the models, 5−7 iterations are required for the full GQME approach.

An inhomogeneous term is only required for the acceptor single-population GQME approach and would be required for any GQME approach where the set of electronic states that it projects onto does not include the initial electronic state. Because of the scaling of the Volterra algorithm for the
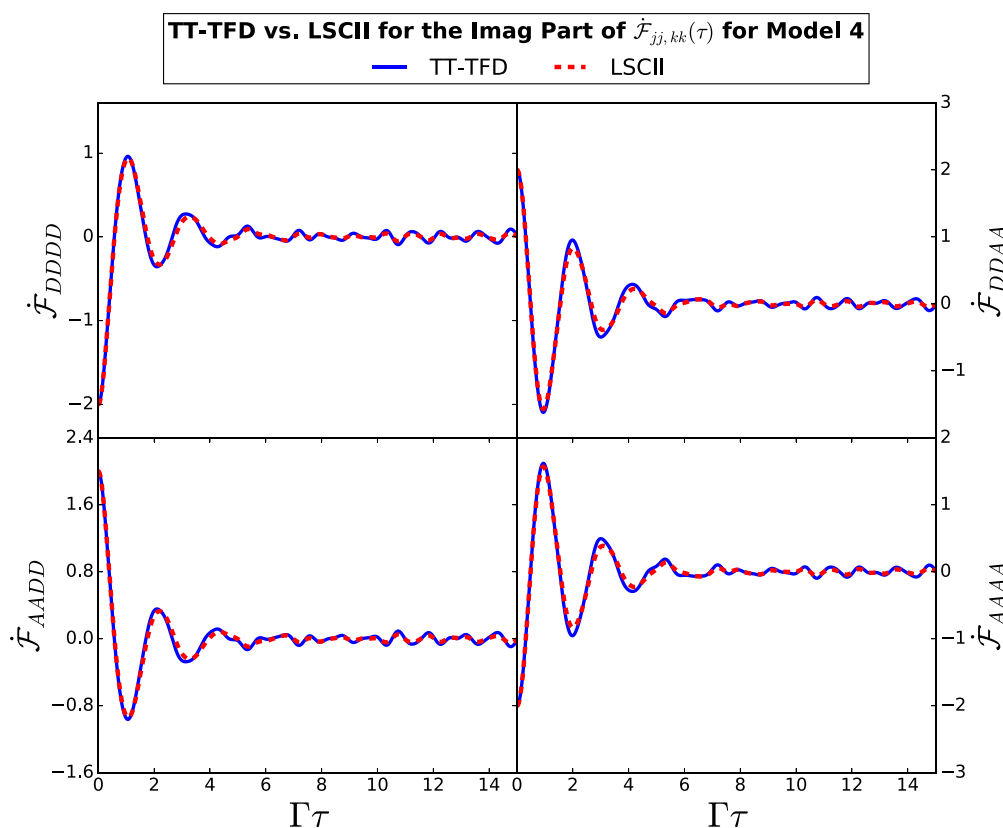
Figure 10. Imaginary parts of the DDDD, DDAA, AADD, and AAAA matrix elements of $\dot{\mathcal{F}}(\tau)$ (see eq 12) for model 4, as obtained via TT-TFD (solid blue lines) and LSCII (dashed red lines). Similar graphs for the other four models are included in the SI.

Table 2. Memory Time of Each GQME Approach for Each Model[a]

Model #	Input Method	Full GQME	Populations-Only GQME	Donor GQME	Acceptor GQME
1	TT-TFD	5.5034	14.7534	14.7534	14.5034
1	LSCII	5.25415	14.7541	14.5041	14.5041
2	TT-TFD	1.65348	14.4035	14.9035	14.4035
2	LSCII	3.00415	14.2541	14.2541	14.2541
3	TT-TFD	9.5034	13.7534	13.5034	14.0034
3	LSCII	7.25415	9.25415	12.0041	11.5041
4	TT-TFD	14.6539	5.65386	14.9039	11.9039
4	LSCII	4.00415	5.75415	13.5041	8.75415
6	TT-TFD	9.65348	10.4035	13.9035	13.6535
6	LSCII	12.7541	14.7541	14.2541	13.5041

[a]In this table, the colors are to provide a visual aid, with red indicating a memory time above 12 Γ^{-1}, yellow indicating a memory time from 9−12 Γ^{-1}, and green indicating a memory time below 9 Γ^{-1}.

inhomogeneous term, it is generally only favorable to use a GQME approach that requires an inhomogeneous term when the dimensionality of the set of electronic states projected onto is small.

The converged memory time for each of the models and GQME types is found using the algorithm outlined in the SI of ref 19. The basic premise of the algorithm is to first calculate the dynamics at the highest possible memory time, $t_{\mathrm{mem,max}}$, based on the maximum time of the PFI dynamics and then proceed backward in memory time to find the shortest memory time that keeps each element and time step of the electronic density matrix within a convergence parameter when compared to the same element and time step of the dynamics

with the highest possible memory time. For the models studied in this paper, the highest possible memory time was $t_{\mathrm{mem,max}} = 15\ \Gamma^{-1}$. The converged memory time for each model and GQME approach is given in Table 2. In agreement with the results for LSCII in ref 19, the full GQME typically corresponds to the shortest memory time and the reduced-dimensionality GQMEs require significantly longer memory times, particularly the single-population GQMEs. Whereas the RK4 algorithm is expected to have computational complexity $O(t_{\mathrm{mem}})$, the cost of a single iteration of the Volterra algorithm for the memory kernel has quadratic computational complexity $O(t_{\mathrm{mem}}^2)$. Thus, situations where the reduced dimensionality of

the electronic observable of interest leads to longer memory time increase the computational cost.

The computational cost of the GQME approaches, with respect to dimensionality, is therefore dependent on several factors with different and, at times, opposing scaling trends. Thus, the computational cost benefits of reduced-dimensionality GQMEs are dependent on the balance between these trends, and further work is needed to determine whether using a reduced-dimensionality GQME provides a way to significantly reduce computational cost.

6. CONCLUDING REMARKS

We have implemented the TT-TFD method to obtain quantum-mechanically exact memory kernels and inhomogeneous terms for different types of GQMEs that describe the dynamics of electronic DOF for the spin-boson model. We have analyzed a GQME for the four-element full electronic reduced density matrix, a populations-only GQME for the two diagonal elements, and single-population scalar GQMEs for single diagonal elements. We have also demonstrated that all four GQMEs are exact equations of motion and thus reproduce the same exact population dynamics when parametrized by a quantum-mechanically exact input method such as TT-TFD, although the four GQMEs are different in form and dimensionality.

Advancing the capability to calculate quantum-mechanically exact memory kernels and inhomogeneous terms for different types of GQMEs is highly desirable for multiple reasons:

- First, note that the memory kernels and inhomogeneous terms in the case of quantum open systems serve a similar role to that of the Hamiltonian in the case of closed quantum systems. More specifically, similar to how analyzing the properties of the Hamiltonian is often used to shed light on the closed quantum system dynamics it gives rise to, one expects that knowing what the quantum-mechanically exact memory kernel and inhomogeneous term look like and how they depend on various parameters and different choices of projections could shed light on the open quantum system dynamics they give rise to.

- Second, quantum-mechanically exact memory kernels and inhomogeneous terms are particularly valuable to evaluate the capabilities of PFIs obtained with approximate input methods, as shown in our comparisons of memory kernels and inhomogeneous terms obtained with exact TT-TFD and approximate LSCII simulation methods.

- Third, quantum-mechanically exact memory kernels can be used as benchmarks to assess the accuracy of various types of perturbative quantum master equations (QMEs).[73−84] More specifically, while the GQMEs correspond to the exact equations of motion of the subset of dynamical quantities of interest, the derivation of perturbative QMEs relies on approximate expressions for the memory kernels that are based on treating various terms in the Hamiltonian, such as the system-bath coupling or electronic coupling, as small perturbations. Thus, comparisons of the perturbative memory kernels to the exact kernels can provide a better understanding of the accuracy of perturbative methods and their range of validity.

- Fourth, in certain situations, simulating the quantum dynamics via a GQME may be more cost-effective than the direct use of the numerically exact quantum dynamics method. More specifically, restricting the use of a quantum-mechanically exact method with regard to calculating the PFIs can provide a more efficient route to obtain the dynamics of the quantity of interest, compared to extracting it from the overall system dynamics. The computational cost analysis of the TT-TFD-based GQME approach provided in this paper constitutes an important step toward understanding when and how simulating the quantum dynamics via a GQME approach is advantageous, compared to the direct use of the numerically exact quantum dynamics method.

Various extensions of this study would be highly desirable, including combining the GQME approach with other quantum-mechanically exact and approximate input methods, calculating memory kernels and inhomogeneous terms for other types of dynamical quantities of interest, and exploring the capabilities of the GQMEs on other benchmark models. Work on such extensions is currently underway and will be reported in future publications.

■ ASSOCIATED CONTENT

Data Availability Statement

The code for the TT-TFD + GQME simulation of Model 1 is available at https://github.com/NingyiLyu/TT-TFD-GQME. The data that supports the findings of this study are available within the article and SI.

Ⓢ Supporting Information

The Supporting Information is available free of charge at https://pubs.acs.org/doi/10.1021/acs.jctc.2c00892.

> Thorough derivation of the GQME reduced-dimensionality approach and a description of the linear combinations used within the TT-TFD approach to obtain elements of the time evolution operator of the reduced electronic density operator, $\mathcal{U}(t)$, for off-diagonal initial states, along with graphs of the PFIs, memory kernels, and inhomogeneous terms (PDF)

■ AUTHOR INFORMATION

Corresponding Authors

Eitan Geva − *Department of Chemistry, University of Michigan, Ann Arbor, Michigan 48109, United States;* Ⓞ orcid.org/0000-0002-7935-4586; Email: eitan@umich.edu

Victor S. Batista − *Department of Chemistry, Yale University, New Haven, Connecticut 06520, United States; Yale Quantum Institute, Yale University, New Haven, Connecticut 06511, United States;* Ⓞ orcid.org/0000-0002-3262-1237; Email: victor.batista@yale.edu

Authors

Ningyi Lyu − *Department of Chemistry, Yale University, New Haven, Connecticut 06520, United States;* Ⓞ orcid.org/0000-0001-9239-9925

Ellen Mulvihill − *Department of Chemistry, Yale University, New Haven, Connecticut 06520, United States;* Ⓞ orcid.org/0000-0002-4233-2869

Micheline B. Soley − *Department of Chemistry, Yale University, New Haven, Connecticut 06520, United States;*

Yale Quantum Institute, Yale University, New Haven, Connecticut 06511, United States; Department of Chemistry, University of Wisconsin–Madison, Madison, Wisconsin 53706, United States; ⦿ orcid.org/0000-0001-7973-2842

Author Contributions

▽These authors contributed equally.

Notes

The authors declare no competing financial interest.

■ REFERENCES

(1) Xu, D.; Schulten, K. Coupling of protein motion to electron transfer in a photosynthetic reaction center: investigating the low temperature behavior in the framework of the spin–boson model. *Chem. Phys.* **1994**, *182*, 91–117.

(2) Ishizaki, A.; Fleming, G. R. Quantum Coherence in Photosynthetic Light Harvesting. *Annu. Rev. Condens. Matter Phys.* **2012**, *3*, 333–361.

(3) Liddell, P. A.; Kuciauskas, D.; Sumida, J. P.; Nash, B.; Nguyen, D.; Moore, A. L.; Moore, T. A.; Gust, D. Photoinduced charge separation and charge recombination to a triplet state in a carotene-porphyrin-fullerene triad. *J. Am. Chem. Soc.* **1997**, *119*, 1400–1405.

(4) Liddell, P. A.; Kodis, G.; Moore, A. L.; Moore, T. A.; Gust, D. Photo switching of photoinduced electron transfer in a dithienyle-thene-porphyrin-fullerene triad molecule. *J. Am. Chem. Soc.* **2002**, *124*, 7668–7669.

(5) Brédas, J.-L.; Beljonne, D.; Coropceanu, V.; Cornil, J. Charge-Transfer and Energy-Transfer Processes in π-Conjugated Oligomers and Polymers: A Molecular Picture. *Chem. Rev.* **2004**, *104*, 4971–5004.

(6) Rizzi, A. C.; van Gastel, M.; Liddell, P. A.; Palacios, R. E.; Moore, G. F.; Kodis, G.; Moore, A. L.; Moore, T. A.; Gust, D.; Braslavsky, S. E. Entropic changes control the charge separation process in triads mimicking photosynthetic charge separation. *J. Phys. Chem. A* **2008**, *112*, 4215–4223.

(7) Tian, H.; Yu, Z.; Hagfeldt, A.; Kloo, L.; Sun, L. Organic Redox Couples and Organic Counter Electrode for Efficient Organic Dye-Sensitized Solar Cells. *J. Am. Chem. Soc.* **2011**, *133*, 9413–9422.

(8) Mishra, A.; Fischer, M. K. R.; Bäuerle, P. Metal-Free Organic Dyes for Dye-Sensitized Solar Cells: From Structure: Property Relationships to Design Rules. *Angew. Chem., Int. Ed.* **2009**, *48*, 2474–2499.

(9) Feldt, S. M.; Gibson, E. A.; Gabrielsson, E.; Sun, L.; Boschloo, G.; Hagfeldt, A. Design of Organic Dyes and Cobalt Polypyridine Redox Mediators for High-Efficiency Dye-Sensitized Solar Cells. *J. Am. Chem. Soc.* **2010**, *132*, 16714–16724.

(10) Zhao, Y.; Liang, W. Charge transfer in organic molecules for solar cells: Theoretical perspective. *Chem. Soc. Rev.* **2012**, *41*, 1075–1087.

(11) Lee, M. H.; Dunietz, B. D.; Geva, E. Calculation From First Principles of Intramolecular Golden-Rule Rate Constants for Photo-Induced Electron Transfer in Molecular Donor-Acceptor Systems. *J. Phys. Chem. C* **2013**, *117*, 23391–23401.

(12) Lee, M. H.; Dunietz, B. D.; Geva, E. Donor-to-Donor vs. Donor-to-Acceptor Interfacial Charge Transfer States in the Phthalocyanine-Fullerene Organic Photovoltaic System. *J. Phys. Chem. Lett.* **2014**, *5*, 3810–3816.

(13) Leggett, A. J.; Chakravarty, S.; Dorsey, A. T.; Fisher, M. P. A.; Garg, A.; Zwerger, W. Dynamics of the dissipative two-state system. *Rev. Mod. Phys.* **1987**, *59*, 1–85.

(14) Breuer, H.-P.; Petruccione, F. *The Theory of Open Quantum Systems*; Oxford Press: Oxford, U.K., 2002.

(15) Nitzan, A. *Chemical Dynamics in Condensed Phases*; Oxford University Press: New York, 2006.

(16) Weiss, U. *Quantum Dissipative Systems*, 4th Edition; World Scientific, 2012.

(17) Nakajima, S. On the quantum theory of transport phenomena. *Prog. Theor. Phys.* **1958**, *20*, 948–959.

(18) Zwanzig, R. Ensemble method in the theory of irreversibility. *J. Chem. Phys.* **1960**, *33*, 1338–1341.

(19) Mulvihill, E.; Geva, E. Simulating the dynamics of electronic observables via reduced-dimensionality generalized quantum master equations. *J. Chem. Phys.* **2022**, *156*, 044119.

(20) Meyer, H.-D.; Gatti, F.; Worth, G. A. *Multidimensional Quantum Dynamics; MCTDH Theory and Applications*; John Wiley & Sons, 2009.

(21) Makri, N. Time-dependent quantum methods for large systems. *Annu. Rev. Phys. Chem.* **1999**, *50*, 167.

(22) Jin, J.; Zheng, X.; Yan, Y. Exact dynamics of dissipative electronic systems and quantum transport: Hierarchical equations of motion approach. *J. Chem. Phys.* **2008**, *128*, 234703–16.

(23) Tanimura, Y.; Kubo, R. Time evolution of a quantum system in contact with a nearly Gaussian-Markoffian noise bath. *J. Phys. Soc. Jpn.* **1989**, *58*, 101.

(24) Tanimura, Y. Nonperturbative expansion method for a quantum system coupled to a harmonic-oscillator bath. *Phys. Rev. A* **1990**, *41*, 6676–6687.

(25) Tanimura, Y. Stochastic Liouville, Langevin, Fokker–Planck, and Master Equation Approaches to Quantum Dissipative Systems. *J. Phys. Soc. Jpn.* **2006**, *75*, 082001.

(26) Greene, S. M.; Batista, V. S. Tensor-Train Split-Operator Fourier Transform (TT-SOFT) Method: Multidimensional Nonadiabatic Quantum Dynamics. *J. Chem. Theory Comput.* **2017**, *13*, 4034–4042.

(27) Shi, Q.; Geva, E. A new approach to calculating the memory kernel of the generalized quantum master equation for an arbitrary system-bath coupling. *J. Chem. Phys.* **2003**, *119*, 12063–12076.

(28) Shi, Q.; Geva, E. A semiclassical generalized quantum master equation for an arbitrary system-bath coupling. *J. Chem. Phys.* **2004**, *120*, 10647–10658.

(29) Zhang, M.-L.; Ka, B. J.; Geva, E. Nonequilibrium quantum dynamics in the condensed phase via the generalized quantum master equation. *J. Chem. Phys.* **2006**, *125*, 044106–12.

(30) Ka, B. J.; Zhang, M.-L.; Geva, E. Homogeneity and Markovity of electronic dephasing in liquid solutions. *J. Chem. Phys.* **2006**, *125*, 124509.

(31) Cohen, G.; Rabani, E. Memory effects in nonequilibrium quantum impurity models. *Phys. Rev. B* **2011**, *84*, 075150.

(32) Wilner, E. Y.; Wang, H.; Cohen, G.; Thoss, M.; Rabani, E. Bistability in a nonequilibrium quantum system with electron-phonon interactions. *Phys. Rev. B* **2013**, *88*, 045137.

(33) Cohen, G.; Wilner, E. Y.; Rabani, E. Generalized projected dynamics for non-system observables of non-equilibrium quantum impurity models. *New J. Phys.* **2013**, *15*, 073018.

(34) Cohen, G.; Gull, E.; Reichman, D. R.; Millis, A. J.; Rabani, E. Numerically exact long-time magnetization dynamics at the nonequilibrium Kondo crossover of the Anderson impurity model. *Phys. Rev. B* **2013**, *87*, 195108.

(35) Kelly, A.; Markland, T. E. Efficient and accurate surface hopping for long time nonadiabatic quantum dynamics. *J. Chem. Phys.* **2013**, *139*, 014104–10.

(36) Kidon, L.; Wilner, E. Y.; Rabani, E. Exact calculation of the time convolutionless master equation generator: Application to the nonequilibrium resonant level model. *J. Chem. Phys.* **2015**, *143*, 234110−9.

(37) Pfalzgraff, W. C.; Kelly, A.; Markland, T. E. Nonadiabatic Dynamics in Atomistic Environments: Harnessing Quantum-Classical Theory with Generalized Quantum Master Equations. *J. Phys. Chem. Lett.* **2015**, *6*, 4743−4748.

(38) Montoya-Castillo, A.; Reichman, D. R. Approximate but accurate quantum dynamics from the Mori formalism: I. Non-equilibrium dynamics. *J. Chem. Phys.* **2016**, *144*, 184104−16.

(39) Kelly, A.; Brackbill, N.; Markland, T. E. Accurate nonadiabatic quantum dynamics on the cheap: Making the most of mean field theory with master equations. *J. Chem. Phys.* **2015**, *142*, 094110−9.

(40) Kelly, A.; Montoya-Castillo, A.; Wang, L.; Markland, T. E. Generalized quantum master equations in and out of equilibrium: When can one win? *J. Chem. Phys.* **2016**, *144*, 184105.

(41) Kidon, L.; Wang, H.; Thoss, M.; Rabani, E. On the memory kernel and the reduced system propagator. *J. Chem. Phys.* **2018**, *149*, 104105.

(42) Pfalzgraff, W.; Montoya-Castillo, A.; Kelly, A.; Markland, T. Efficient construction of generalized master equation memory kernels for multi-state systems from nonadiabatic quantum-classical dynamics. *J. Chem. Phys.* **2019**, *150*, 244109.

(43) Mulvihill, E.; Schubert, A.; Sun, X.; Dunietz, B. D.; Geva, E. A modified approach for simulating electronically nonadiabatic dynamics via the generalized quantum master equation. *J. Chem. Phys.* **2019**, *150*, 034101.

(44) Mulvihill, E.; Gao, X.; Liu, Y.; Schubert, A.; Dunietz, B. D.; Geva, E. Combining the mapping Hamiltonian linearized semiclassical approach with the generalized quantum master equation to simulate electronically nonadiabatic molecular dynamics. *J. Chem. Phys.* **2019**, *151*, 074103.

(45) Mulvihill, E.; Lenn, K. M.; Gao, X.; Schubert, A.; Dunietz, B. D.; Geva, E. Simulating energy transfer dynamics in the Fenna-Matthews-Olson complex via the modified generalized quantum master equation. *J. Chem. Phys.* **2021**, *154*, 204109.

(46) Mulvihill, E.; Geva, E. A Road Map to Various Pathways for Calculating the Memory Kernel of the Generalized Quantum Master Equation. *J. Phys. Chem. B* **2021**, *125*, 9834−9852.

(47) Xu, M.; Yan, Y.; Liu, Y.; Shi, Q. Convergence of high order memory kernels in the Nakajima−Zwanzig generalized master equation and rate constants: Case study of the spin-boson model. *J. Chem. Phys.* **2018**, *148*, 164101.

(48) Liu, Y.-y.; Yan, Y.-m.; Xu, M.; Song, K.; Shi, Q. Exact generator and its high order expansions in time-convolutionless generalized master equation: Applications to spin-boson model and excitation energy transfer. *Chin. J. Chem. Phys.* **2018**, *31*, 575−583.

(49) Yan, Y.; Xu, M.; Liu, Y.; Shi, Q. Theoretical study of charge carrier transport in organic molecular crystals using the Nakajima-Zwanzig-Mori generalized master equation. *J. Chem. Phys.* **2019**, *150*, 234101.

(50) Dan, X.; Xu, M.; Yan, Y.; Shi, Q. Generalized master equation for charge transport in a molecular junction: Exact memory kernels and their high order expansion. *J. Chem. Phys.* **2022**, *156*, 134114.

(51) Chatterjee, S.; Makri, N. Real-Time Path Integral Methods, Quantum Master Equations, and Classical vs Quantum Memory. *J. Phys. Chem. B* **2019**, *123*, 10470−10482.

(52) Brian, D.; Sun, X. Generalized quantum master equation: A tutorial review and recent advances. *Chin. J. Chem. Phys.* **2021**, *34*, 497−524.

(53) Gelin, M. F.; Borrelli, R. Thermal Schrödinger Equation: Efficient Tool for Simulation of Many-Body Quantum Dynamics at Finite Temperature. *Ann. Phys.* **2017**, *529*, 1700200.

(54) Borrelli, R.; Gelin, M. F. Finite temperature quantum dynamics of complex systems: Integrating thermo-field theories and tensor-train methods. *WIREs Comput. Mol. Sci.* **2021**, *11*, No. e1539.

(55) Ng, N.; Limmer, D. T.; Rabani, E. Nonuniqueness of generalized quantum master equations for a single observable. *J. Chem. Phys.* **2021**, *155*, 156101.

(56) Wang, Y.; Mulvihill, E.; Hu, Z.; Lyu, N.; Shivpuje, S.; Liu, Y.; Soley, M. B.; Geva, E.; Batista, V. S.; Kais, S. Submitted. https://arxiv.org/abs/2209.04956

(57) Borrelli, R.; Gelin, M. F. Quantum electron-vibrational dynamics at finite temperature: Thermo field dynamics approach. *J. Chem. Phys.* **2016**, *145*, 224101.

(58) Borrelli, R.; Gelin, M. F. Simulation of Quantum Dynamics of Excitonic Systems at Finite Temperature: An efficient method based on Thermo Field Dynamics. *Sci. Rep.* **2017**, *7*, DOI: 10.1038/s41598-017-08901-2.

(59) Oseledets, I. V. Tensor-train decomposition. *SIAM J. Sci. Comput.* **2011**, *33*, 2295−2317.

(60) Oseledets, I.; Tyrtyshnikov, E. TT-cross approximation for multidimensional arrays. *Linear Algebra Appl.* **2010**, *432*, 70−88.

(61) Grasedyck, L. Hierarchical singular value decomposition of tensors. *SIAM J. Matrix Anal. Appl.* **2010**, *31*, 2029−2054.

(62) Hackbusch, W.; Kühn, S. A new scheme for the tensor representation. *J. Fourier Anal. Appl.* **2009**, *15*, 706−722.

(63) Lyu, N.; Soley, M. B.; Batista, V. S. Tensor-Train Split-Operator KSL (TT-SOKSL) Method for Quantum Dynamics Simulations. *J. Chem. Theory Comput.* **2022**, *18*, 3327−3346.

(64) Soley, M. B.; Bergold, P.; Gorodetsky, A. A.; Batista, V. S. Functional Tensor-Train Chebyshev Method for Multidimensional Quantum Dynamics Simulations. *J. Chem. Theory Comput.* **2022**, *18*, 25−36.

(65) Soley, M. B.; Bergold, P.; Batista, V. S. Iterative Power Algorithm for Global Optimization with Quantics Tensor Trains. *J. Chem. Theory Comput.* **2021**, *17*, 3280−3291.

(66) Takahashi, Y.; Umezawa, H. Thermo Field Dynamics. *Int. J. Mod. Phys. B* **1996**, *10*, 1755−1805.

(67) Lubich, C.; Oseledets, I. V.; Vandereycken, B. Time integration of tensor trains. *SIAM J. Num. Anal.* **2015**, *53*, 917−941.

(68) Lubich, C.; Oseledets, I. V. A projector-splitting integrator for dynamical low-rank approximation. *BIT Num. Math.* **2014**, *54*, 171−188.

(69) Li, W.; Ren, J.; Shuai, Z. Numerical assessment for accuracy and GPU acceleration of TD-DMRG time evolution schemes. *J. Chem. Phys.* **2020**, *152*, 024127.

(70) Sun, X.; Wang, H.; Miller, W. H. On the semiclassical description of quantum coherence in thermal rate constants. *J. Chem. Phys.* **1998**, *109*, 4190−4200.

(71) Saller, M. A. C.; Lai, Y.; Geva, E. An Accurate Linearized Semiclassical Approach for Calculating Cavity-Modified Charge Transfer Rate Constants. *J. Phys. Chem. Lett.* **2022**, *13*, 2330−2337.

(72) Ren, J.; Li, W.; Jiang, T.; Wang, Y.; Shuai, Z. Time-dependent density matrix renormalization group method for quantum dynamics in complex systems. *WIREs: Comput. Mol. Sci.* **2022**, *12*, e1614.

(73) Baiz, C. R.; Kubarych, K. J.; Geva, E. Molecular theory and simulation of coherence transfer in metal carbonyls and its signature on multidimensional infrared spectra. *J. Phys. Chem. B* **2011**, *115*, 5322−5339.

(74) Redfield, A. G. On the theory of relaxation processes. *IBM J.* **1957**, *1*, 19.

(75) Pollard, W. T.; Friesner, R. A. Solution of the Redfield equation for the dissipative quantum dynamics of multilevel systems. *J. Chem. Phys.* **1994**, *100*, 5054.

(76) Pollard, W. T.; Felts, A. K.; Friesner, R. A. The Redfield equation in condensed-phase quantum dynamics. *Adv. Chem. Phys.* **2007**, *XCIII*, 77.

(77) Meier, C.; Tannor, D. Non-Markovian evolution of the density operator in presence of strong laser fields. *J. Chem. Phys.* **1999**, *111*, 3365.

(78) Egorova, D.; Kühl, A.; Domcke, W. Modeling of ultrafast electron-transfer dynamics: Multi-level Redfield theory and validity of approximation. *Chem. Phys.* **2001**, *268*, 105.

(79) Laird, B. B.; Budimir, J.; Skinner, J. L. *J. Chem. Phys.* **1991**, *94*, 4391.

(80) Zhang, W. M.; Meier, T.; Chernyak, V.; Mukamel, S. Exciton-migration and three-pulse femtosecond optical spectroscopies of photosynthetic antenna complexes. *J. Chem. Phys.* **1998**, *108*, 7763−7774.

(81) Novoderezhkin, V. I.; Yakovlev, A. G.; van Grondelle, R.; Shuvalov, V. A. Coherent Nuclear and Electronic Dynamics in Primary Charge Separation in Photosynthetic Reaction Centers: A Redfield Theory Approach. *J. Phys. Chem. B* **2004**, *108*, 7445−7457.

(82) Trushechkin, A. Calculation of coherences in Förster and modified Redfield theories of excitation energy transfer. *J. Chem. Phys.* **2019**, *151*, 074101−19.

(83) Jang, S. J. *Dynamics of Molecular Excitons*; Elsevier, 2020.

(84) Lai, Y.; Geva, E. On simulating the dynamics of electronic populations and coherences via quantum master equations based on treating off-diagonal electronic coupling terms as a small perturbation. *J. Chem. Phys.* **2021**, *155*, 204101.

📖 Recommended by ACS

Path Integral over Equivalence Classes for Quantum Dynamics with Static Disorder

Nancy Makri.

JANUARY 31, 2024

THE JOURNAL OF PHYSICAL CHEMISTRY LETTERS   READ 🗗

Stochastic Schrödinger Equation Approach to Real-Time Dynamics of Anderson–Holstein Impurities: An Open Quantum System Perspective

Zhen Huang, Zhennan Zhou, *et al.*

JANUARY 09, 2024

JOURNAL OF CHEMICAL THEORY AND COMPUTATION   READ 🗗

Simulating Open Quantum System Dynamics on NISQ Computers with Generalized Quantum Master Equations

Yuchen Wang, Sabre Kais, *et al.*

MAY 26, 2023

JOURNAL OF CHEMICAL THEORY AND COMPUTATION   READ 🗗

Hamiltonian Learning from Time Dynamics Using Variational Algorithms

Rishabh Gupta, Sabre Kais, *et al.*

MARCH 29, 2023

THE JOURNAL OF PHYSICAL CHEMISTRY A   READ 🗗

Get More Suggestions >